J. Fluid Mech. (2008), *vol.* 606, *pp.* 153–188.
doi:10.1017/S0022112008001699 Printed in the United Kingdom

The naturally oscillating flow emerging from a fluidic precessing jet nozzle

CHONG Y. WONG†, GRAHAM J. NATHAN AND RICHARD M. KELSO

School of Mechanical Engineering, University of Adelaide, Adelaide, South Australia 5005, Australia

(Received 23 April 2007 and in revised form 10 March 2008)

Phase-averaged and directionally triggered digital particle image velocimetry measurements were taken in longitudinal and transverse planes in the near field of the flow emerging from a fluidic precessing jet nozzle. Measurements were performed at nozzle inlet Reynolds and Strouhal numbers of 59 000 and 0.0017, respectively. Results indicate that the jet emerging from the nozzle departs with an azimuthal component in a direction opposite to that of the jet precession. In addition, the structure of the 'flow convergence' region, reported in an earlier study, is better resolved here. At least three unique vortex-pair regions containing smaller vortical 'blobs' are identified for the first time. These include a vortex-pair region originating from the foci on the downstream face of the nozzle centrebody, a vortex-pair region shed from the edge of the centrebody and a vortex-pair region originating from the downstream surface of the nozzle exit lip.

1. Introduction

Unsteady precessing flow instabilities can occur within an axisymmetric nozzle of appropriate geometrical dimensions. These flows are of fundamental interest because the mechanisms which generate them are still poorly understood. Their occurrence can be undesirable in applications such as milk driers (Guo, Langrish & Fletcher 2001) and the precessing vortex cores in swirl-stabilized combustion chambers (Syred 2006). However, the precessing jet flow can offer significant advantages in the combustion of gaseous (Nathan, Luxton & Smart 1992; Manias & Nathan 1994) and particulate fuels (Smith *et al.* 1998), notably in applications such as rotary kilns where high radiant heat transfer and low NO_x emissions are desired. Nathan *et al.* (2006) shows that precessing jet flows lead to reduced global flame strain rates within flames, relative to other flows commonly used in burners, which increases the volume of soot within the flame. Since soot dominates incandescent radiation from gaseous flames, this acts both to increase heat transfer by radiation and to reduce the flame temperature, so reducing NO_x emissions by the thermal route. Over the years, much has been learned about this complex flow. However, key details of the underlying mechanism and structure of the external flow have yet to be identified.

Nathan, Hill & Luxton (1998) provide the first detailed report of the configuration of the basic nozzle, referred to herein as the chamber-lip (Ch-L) configuration, that

† Present address: CSIRO Materials Science and Engineering, Commonwealth Scientific and Industrial Research Organisation, Highett, Victoria 3190, Australia

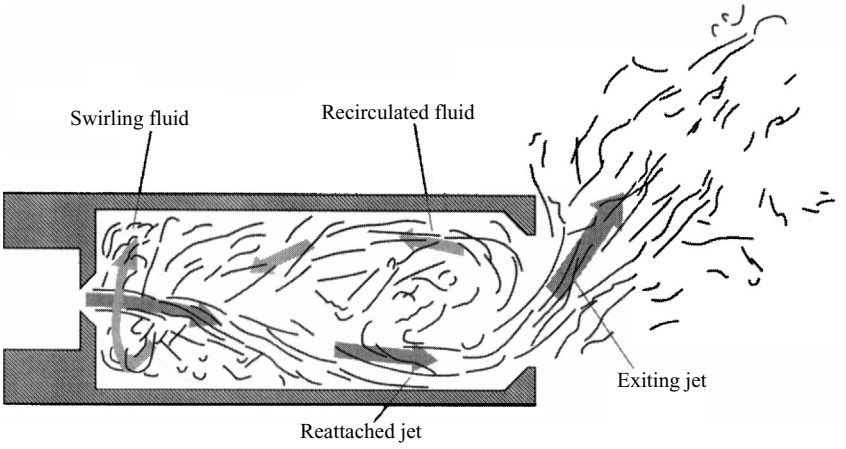

FIGURE 1. Conjectured flow structure of a simple FPJ nozzle comprising an orifice-type inlet and a chamber-lip configuration (Ch-L). $Re_d = 15000$, $D/d = 6.03$, $d = 7.3$ mm, $D_1 = 44$ mm, $L = 114$ mm, $D_2 = 35$ mm (Nathan *et al.* 1998). Reprinted with permission.

produces a precessing jet flow (figure 1). Their investigation reveals the presence of a highly complex and unsteady flow, in which the separated flow within the chamber reattaches asymmetrically within the chamber to produce a large-scale precession of the internal and emerging flows. They deduced key features of the flow based on various flow-visualization techniques, such as china-clay surface flow visualization, coloured dye, bubble and smoke visualizations. They also provided measurements of the oscillation frequency and derived a dimensionless Strouhal number to characterize the oscillation in this configuration, based on a parametric study of the nozzle geometry. However, both the measurements and the visualizations show that there is large cycle-to-cycle variation in the instantaneous flow. Furthermore, the cross-section of the emerging jet is not round (Nathan *et al.* 2006). All of these issues complicate detailed investigation.

To provide insight into this complex flow, a mechanically oscillating jet nozzle was developed in which a round jet is directed at an angle (typically 45°) to an axis about which it is rotated (Schneider *et al.* 1997*a*). This allows independent variation of the controlling parameters. It also allows for an unambiguous definition of the Strouhal number of precession, $St_p = f_p d/u$, where f_p is the frequency of precession, d is the exit orifice diameter and u the exit velocity. At sufficiently low St_p, the trajectory of the jet is almost independent of the precession. However, above a critical value, the precession generates a helical flow in the near field associated with a low-pressure core (Schneider *et al.* 1997*a*). Further increases in St_p produce a gradual tightening of the helix (Mi & Nathan 2005), but provide no substantive changes to the qualitative features. These studies, along with Schneider *et al.* (1997*b*) also reveal that St_p has a much greater influence on the flow than does the Reynolds number ($Re_d = ud/\nu$), where ν is the kinematic viscosity of air. These findings are further supported by the investigation of Nathan, Turns & Bandaru (1996) of the effect of precession on flames from the same nozzle.

Detailed measurements of the external non-reacting and reacting flow from fluidic precessing jet nozzles have also been performed, although there is limited detailed data on the internal and emerging near-field flow. A strong dependence of the flow

on St_p and weak dependence on Re_d have also been consistently found. Note that St_p is essentially determined by the geometry of the nozzle (Mi & Nathan 2004). For a fixed nozzle chamber, St_p is almost independent of Re_d for $Re_d > 20\,000$ (Nathan *et al.* 1998), which is well above the turbulent transition. Newbold (1997) also found the external scalar field to be virtually independent of Re_d in this range. Hence too, the combustion characteristics of flames from a fixed nozzle chamber are effectively independent of Re_d (Newbold, Nathan & Luxton 1997). For this reason, detailed measurements undertaken at one condition can be considered to be broadly representative of the flow through that chamber, if undertaken at sufficiently high Re_d. Parham *et al.* (2005) used planar laser-induced fluorescence in water to assess the effects of confinement and coflow on the scalar field of the non-reacting jet emerging from this nozzle. These measurements, and those of Newbold (1997), show that true precession is present only in the first few chamber diameters. Hence the rapid spread of the emerging jet persists only for a few chamber diameters, and the flow then converges to a far-field flow more like that of a simple jet. In a flame, nearly all of the reaction occurs in this far-field region.

From the flow-visualization results of Nathan *et al.* (1998), Kelso (2001) proposed, through an analytical method, that the internal jet precession is sustained by a 'driving vortex' just downstream from a sudden expansion with a diameter expansion ratio of $D/d = 5$. However, insufficient data for the vortex skeleton within, and emerging from, the chamber is available to assess or refine this model. Likewise, a computational fluid dynamic simulation using a large-eddy simulation was performed for a similar flow, that of a sudden expansion of the same ratio as the precessing jet (PJ) chamber, but into a long pipe at $Re_d = 10^5$, by Guo *et al.* (2001). Again, similar trends were revealed, but insufficient data for the instantaneous unsteady flow field are available for detailed validation. Phase-averaged axial velocities were measured within the chamber, and emerging from it using laser doppler anemometry (LDA) (Wong *et al.* 2003). These confirm the general flow structure observed by the visualization, and provide important flow statistics. However, those experiments did not take into account the azimuthal direction of precession, and LDA, being a single-point technique, is unable to provide details of the phase-averaged vortex patterns in the field of interest.

An improvement to the basic nozzle design (see figure 2) is achieved with the addition of a centrebody (CB) upstream from the nozzle exit to increase the probability of jet precession (Nathan *et al.* 1998). Newbold *et al.* (1995) employed cross-correlation digital particle image velocimetry (DPIV) with a continuous argon-ion laser beam modulated with an acousto-optic modulator to investigate the flow emerging from such a nozzle configuration, termed the chamber-lip-centrebody (Ch-L-CB) arrangement. However, because of the three-dimensional nature of the emerging jet and the constraints of their laser diagnostic technique, their data suffered from severe out-of-plane particle movement, resulting in poor velocity yield, especially in the near field. Hence, no reliable details of the velocity near to the nozzle exit can be obtained from that investigation. Nobes *et al.* (2002) improved on the spatial resolution of the PIV arrangement to provide reliable measurements of the emerging PJ flow. However, since their experiments were not phase-averaged, it also provides only limited further information on the instantaneous structure of the external flow. Wong, Nathan & Kelso (2002) visually sorted their free-running PIV data into either left-sided, or right-sided cases of the emerging jet flow. They reported that the spatially averaged emerging precessing jet has a centreline decay that is more rapid than a free turbulent jet with a uniform initial velocity distribution. However, their results

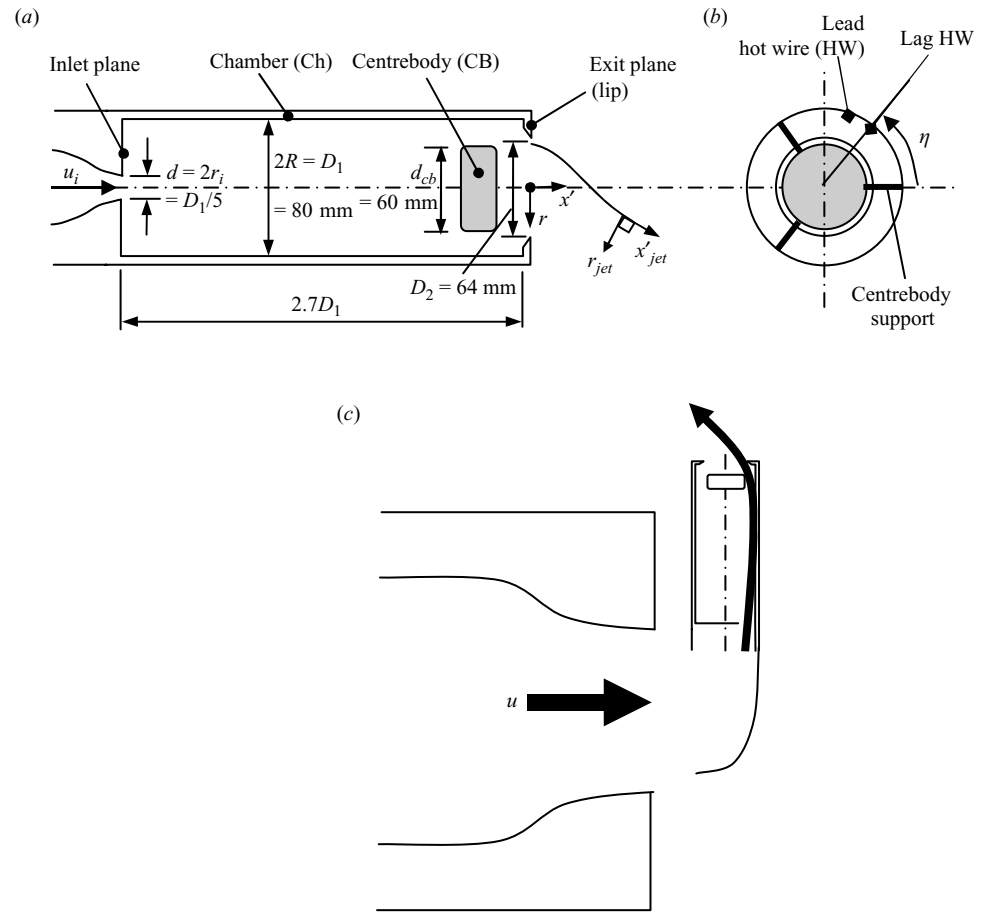

FIGURE 2. Schematic diagram of the experimental nozzle and its placement in the wind tunnel for the steady deflected jet experiments. (*a*) side view, (*b*) end view, (*c*) nozzle positioning for the deflected jet experiments.

also suffered from ambiguities in the direction and phase of the precession of the emerging jet.

The literature is replete with methods used to investigate naturally occurring time-dependent flows (e.g. Steiner & Perry 1987). Often a characteristic feature of the natural oscillation is used to activate a data-collection system. Triggering from a digital PIV data-collection system by pressure probes has been used by Fick, Griffiths & O'Doherty (1997) to study the precessing vortex core (PVC) near the exit of a swirl burner. This was successful in providing measurement of the phase-averaged radial and tangential components of the PVC. A key element to the success of that measurement is that the direction of precession of the PVC is known *a priori*, since it is determined by the swirl geometry. As such, the use of a direction selectivity sensor was not required. In contrast, the direction of precession in the naturally excited fluidic precessing jet changes intermittently, especially for the Ch-L configuration (Nathan 1988). Directional changes in the emerging flow for a Ch-L-CB configuration have also been reported in Wong, Nathan & O'Doherty (2004). The change of azimuthal direction in the related flow of Guo *et al.* (2001) in a long pipe was also numerically

predicted. Hence, to reveal details of the vortex patterns, it is necessary to develop a data collection system that resolves both precession direction and phase.

Nathan *et al.* (1998) found that a high probability of jet precession occurs in a chamber-lip fluidic precessing jet (FPJ) arrangement when the Reynolds number (defined using the velocity, u_i, at the inlet plane) is greater than about 20 000. The jet precession phenomenon has also been verified by Mi, Nathan & Wong (2006) who carried out parametric studies on the chamber-lip arrangement in the Reynolds-number range between 20 000 and 100 000. They also reported that the corresponding peak precession frequency is a proportional function of the Reynolds number for a given configuration. Experiments conducted by Wong *et al.* (2004) at Reynolds numbers of about 100 000 for various configurations of the FPJ nozzle, that is, chamber only (Ch), chamber-lip (Ch-L) and chamber-lip-centrebody (Ch-L-CB) found that fluidic jet precession occurs irrespective of these variations to the nozzle, that is, the phenomenon of fluidic jet precession occurs over a wide range of Reynolds numbers. Furthermore, the Strouhal number is only a weak function of Re_d, and is largely determined by the nozzle geometry (Nathan *et al.* 1998; Mi & Nathan 2004). Therefore the present experiments were conducted at $Re_d = 59\,000$, greater than $Re_d = 20\,000$, to ensure reliable jet precession. Although the introduction of a centrebody further improves the precession reliability, new forms of scaling may be required, as discussed by Mi & Nathan (2004). They proposed several forms of Reynolds- and Strouhal-number scalings, but note that because of the lack of an absolute definition of the nozzle exit velocities and the boundary of the emerging jet, any definition of an external Reynolds or Strouhal number is necessarily subjective. As such, the present investigation defines these numbers based on measurable dimensions such as the diameter of the orifice at the inlet plane (d), bulk velocity at the inlet plane (u_i) and the peak precession frequency (f_p) so that direct comparison can be made with other variants of the FPJ reported in the literature.

To address these issues, the present investigation provides new details of the phase-averaged flow-field emerging from a fluidic precessing jet nozzle. In particular, it aims to identify the key features of the vortex skeleton, the azimuthal component of the emerging jet's trajectory, and the shape of the jet's cross-section. To achieve this, a methodology is developed that allows the emerging precessing jet to be directionally resolved and phase-averaged. The paper is organized into three further sections. Section 2 describes the experimental techniques used, namely, the phase- and direction-triggered PIV system and the surface flow visualization of the components at the nozzle exit plane. Section 3 discusses the results obtained from the transverse (y, z) and the longitudinal (x', r) planes, and observations from the surface flow visualization. Finally, § 4 proposes a feasible flow structure based on the evidence presented in § 3.

2. Experimental techniques

The flow entering the nozzle is conditioned with a diffuser, screens and a smooth contraction, details of which are found in Wong *et al.* (2003). The nozzle chamber has a diameter of $D_1 = 80$ mm and a circular inlet $d = 15.79$ mm (figure 2). A centrebody (thickness, $t_{cb} = 16.8$ mm and diameter, $d_{cb} = 60$ mm) and exit lip (thickness, 2 mm and inner diameter, $D_2 = 64$ mm) are spaced 17.6 mm apart and positioned towards the exit of the nozzle chamber (approximately $2.7D_1$ in length). As mentioned earlier, the centrebody and exit lip improve the reliability of precession and the precessing direction in the jet nozzle (Wong *et al.* 2004).

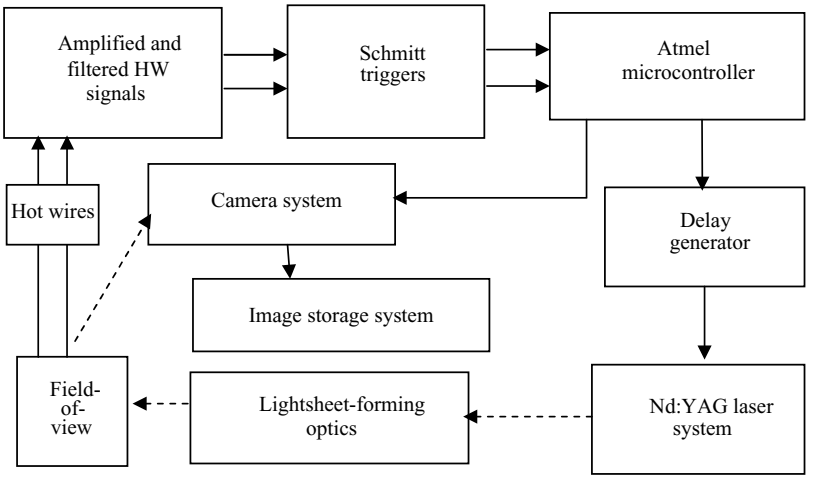

FIGURE 3. Schematic diagram of the PIV system (solid and dashed arrows refer to electrical and light signals, respectively).

2.1. *Phase- and direction-triggered PIV system*

The flow at the inlet plane is seeded with 1 μm olive oil droplets and has a flat velocity distribution (Wong *et al.* 2003, 2004) with a bulk chamber inlet air velocity of $u_i = 55.0\,\mathrm{m\,s^{-1}}$ giving a Reynolds number of $Re_d = 59\,000$. At this velocity, the peak precession frequency, f_p, is approximately 6 Hz, corresponding to a Strouhal number $St_d = 0.0017$ based on u_i and d.

Prior to the present experiments, a parametric series of 11 experimental conditions spanning a Reynolds-number range from 30 000 to 90 000 at a nominal Strouhal number of 0.0017 was conducted in the external longitudinal plane of the FPJ nozzle using time-averaged DPIV with the lightsheet passing though the nozzle axis. Because of the close coupling between Re_d and f_p, an increase in Re_d will correspond to a proportional increase in f_p. The mean velocity distribution across the nozzle exit plane is close to self-similar for all the conditions while fluidic jet precession was also detected by simple pressure sensors positioned between the exit lip and the centrebody. The experimental condition chosen here ($Re_d = 59\,000$, $St_d = 0.0017$) is a mid way point selected from that parametric study.

The phase- and direction-triggered PIV system is described in figure 3. A pair of hot-wire (HW) anemometer probes (each being 1 mm long Wollaston wire of 5 μm nominal diameter) are positioned just downstream from the exit lip. The stationary hot-wire system was designed and manufactured in-house. The centre of the lag HW is located at $x'/D_2 = 0.16$ and $r/D_2 = 0.61$ and is azimuthally offset from the lead HW by 24°. The criterion for selecting this angle was based on the peak precession frequency of the present flow. It was chosen to reduce phase jitter and to reduce the chances of accidental system triggering due to a change in the direction of the precession. Both probes have an overheat ratio of 1.5 and are adjusted to respond equally to the same flow before the offset is applied. Each HW has a frequency response better than 10 kHz, but this value decays after a couple of experimental runs. As such, each wire has to be replaced frequently owing to the build up of olive oil on the active surface of the hot wires. Despite the slightly reduced frequency response, the system is still able to detect the low-frequency precession adequately.

The signals from each HW were low-pass filtered by Krohn-Hite filters (Model 3322) at a cutoff frequency of 30 Hz and passed into respective Schmitt Triggers (STs). These triggers output a high signal (+5 V) each time the filtered signals exceed an arbitrary upper trigger voltage level and they generate a low signal only if the input signal falls below a pre-determined lower trigger level. The trigger ignores any fluctuations in voltage between these two levels. An upper trigger voltage level of 3.33 V was parametrically found to detect most of the dominant precessing flow, while minimizing the detection of non-precessing flows.

The outputs from the Schmitt triggers were fed into the interrupt inputs of an 8-bit Atmel AT90S2313-10PC programmable microcontroller with a frequency resolution of 10 MHz. This controller generated a constant train of 10 Hz pulses to a Stanford Research Systems pulse delay generator (DG-535) which was used to regulate the flashlamps and Q-switch timings of the Nd:YAG laser system.

The microcontroller was programmed to trigger the laser and camera simultaneously on the following conditions. The lag ST must be triggered after the lead ST, the time difference between them must be between 10 and 20 ms (corresponding to a frequency of 6 and 3 Hz, respectively), and these events must occur within 2.5 ms of the next laser clock pulse. In this way, the PIV measurements were conditioned on the flow precessing in a single direction.

The PIV system consisted of a Quantel Brilliant Twins Nd:YAG laser operated at a wavelength of 532 nm and a power of 180 mJ per oscillator output. The output laser beam passed through a series of optical lenses to produce a lightsheet approximately 2 mm thick in the region of interest. A Kodak Megaplus ES1.0 camera, which has an array of 1018×1008 pixels, was used with an AF Zoom-Nikkor 70–300 mm f/4–5.6D ED lens at an f number of 5.6 to provide an estimated depth-of-field of 5.75 mm. Images acquired were transferred to a computer for storage and further processing.

A total of 11 transverse planes ($x'/D_2 = 0.11$, 0.19, 0.27, 0.34, 0.42, 0.50, 0.58, 0.74, 0.89, 1.05 and 1.20) were measured. The time interval between laser pulse, varied with distance downstream from the exit lip. It was 15 μs for $0 < x'/D_2 < 0.58$, 30 μs for $0.58 \leqslant x'/D_2 \leqslant 0.89$ and 20 μs for $x'/D_2 > 0.89$. An interrogation window of 32×32 pixels with a 50 % overlap was used (measurement volume is $6.3\,\text{mm} \times 6.3\,\text{mm} \times 2\,\text{mm}$ nominally). A total of 12 planes ($\eta = 0°$, 15°, 30°, 45°, 60°, 75°, 90°, 105°, 120°, 135°, 150° and 160°) were also interrogated in the longitudinal section, this time using an interrogation window of 16×16 pixels (measurement volume is $1.51\,\text{mm} \times 1.51\,\text{mm} \times 2\,\text{mm}$) and zero overlap. The time interval used here was 15 μs. Velocity fields from all the image pairs were calculated using the cross-correlation and peak detection algorithms of PIVView 1.75 (a commercial software package developed by PIVTec). Spurious vectors, filtered by a global histogram method were removed and replaced by a bi-linear interpolation scheme in the software. Each measurement plane comprised nominally 50 velocity fields, with each field collected at a typical rate of 1 field per 360 cycles of jet precession. The maximum statistical uncertainties for a 95 % confidence interval based on 50 image pairs for the in-plane velocity measurements were also calculated. For measurements in the transverse sections ((y, z)-plane), the largest uncertainties were not more than 3.2 % of the inlet velocity, while the minimum errors were not less than 0.1 %. For measurements in the longitudinal sections ((x', r)-plane), these errors were 2.2 % and 0.08 %, respectively. More details of the uncertainty analysis are found in the Appendix.

Additional surface flow-visualization experiments were also performed at the exit plane and on the downstream face of the centrebody. These additional experiments sought to verify flow features deduced from the PIV experiments.

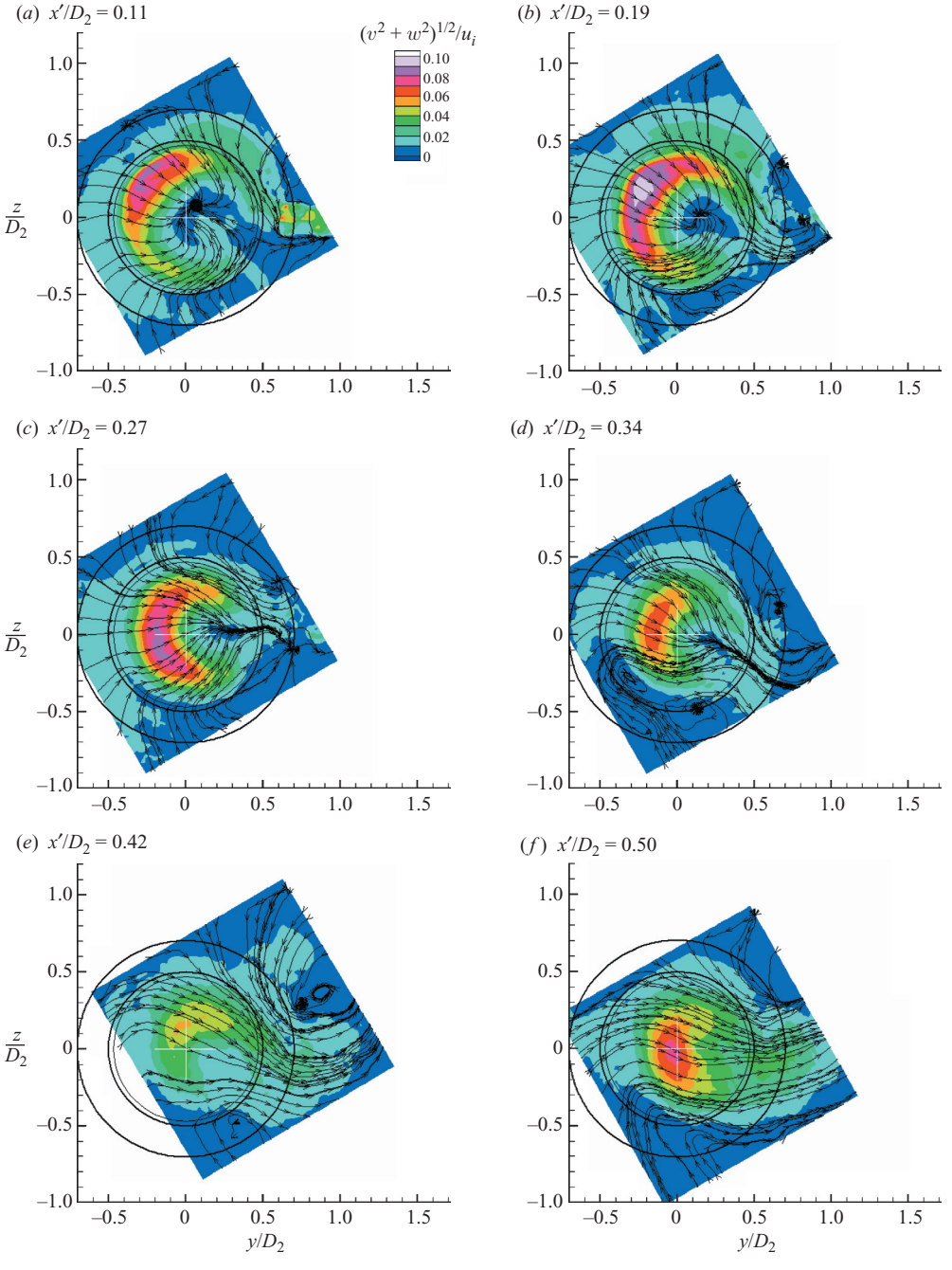

FIGURE 4(*a*–*f*). For caption see facing page.

2.2. *Surface flow-visualization experiments*

Previous flow-visualization studies (e.g. Nathan *et al.* 1998) obtained the time-average features of the freely precessing flow. This provides clues as to the features of the instantaneous pattern, but cannot provide significant insights into the details of the

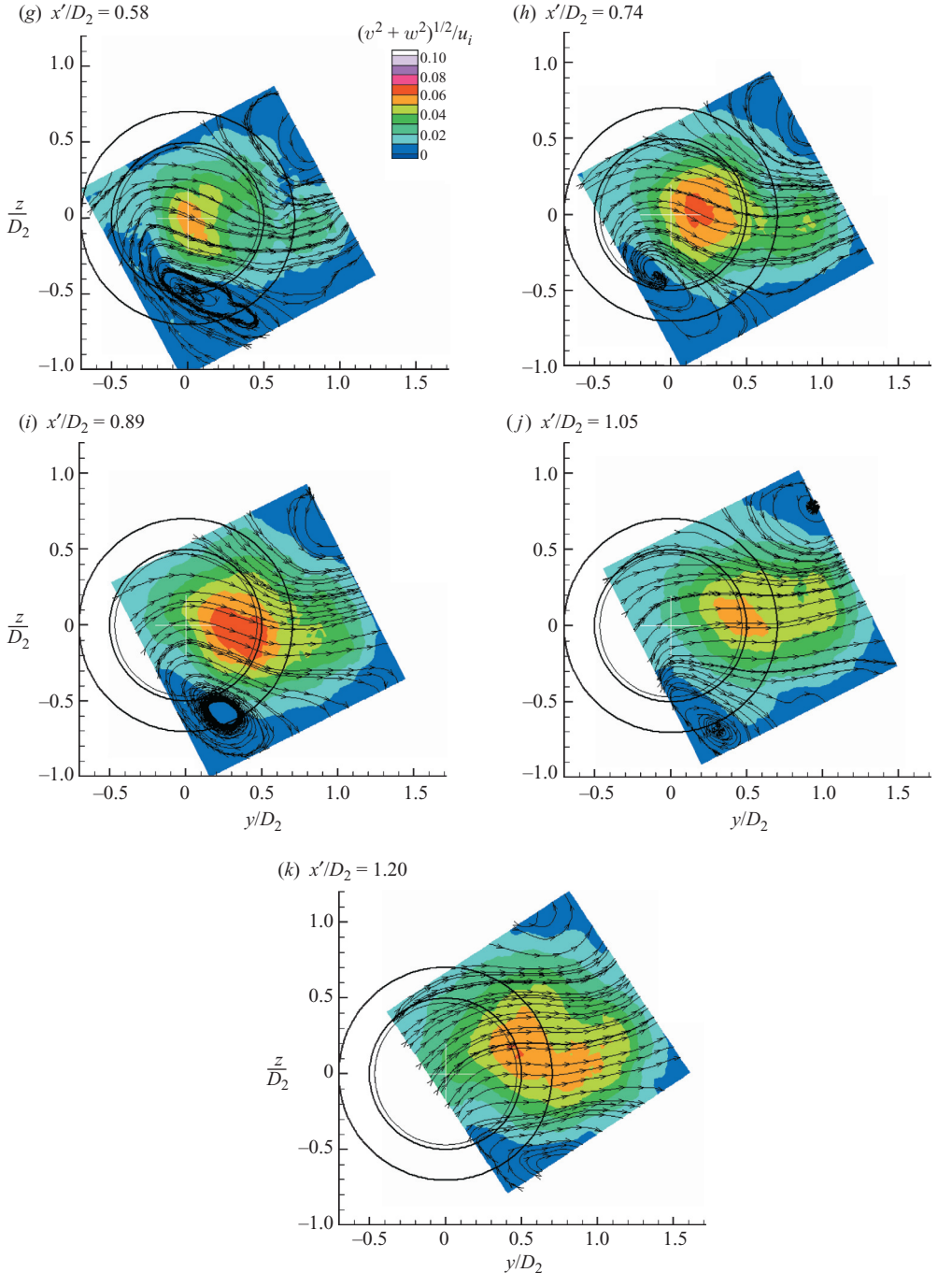

FIGURE 4. Total velocity magnitude $(v^2 + w^2)^{1/2}$ of the phase-direction-triggered PIV in the (y, z)-section when $\eta = 0$ for $x'/D_2 = 0.11$ to 1.20. Streamlines are superimposed onto the coloured contours (normalized velocity magnitude). $Re_d = 59000$, $St_d = 0.0017$. The jet is precessing towards the reader in a clockwise fashion.

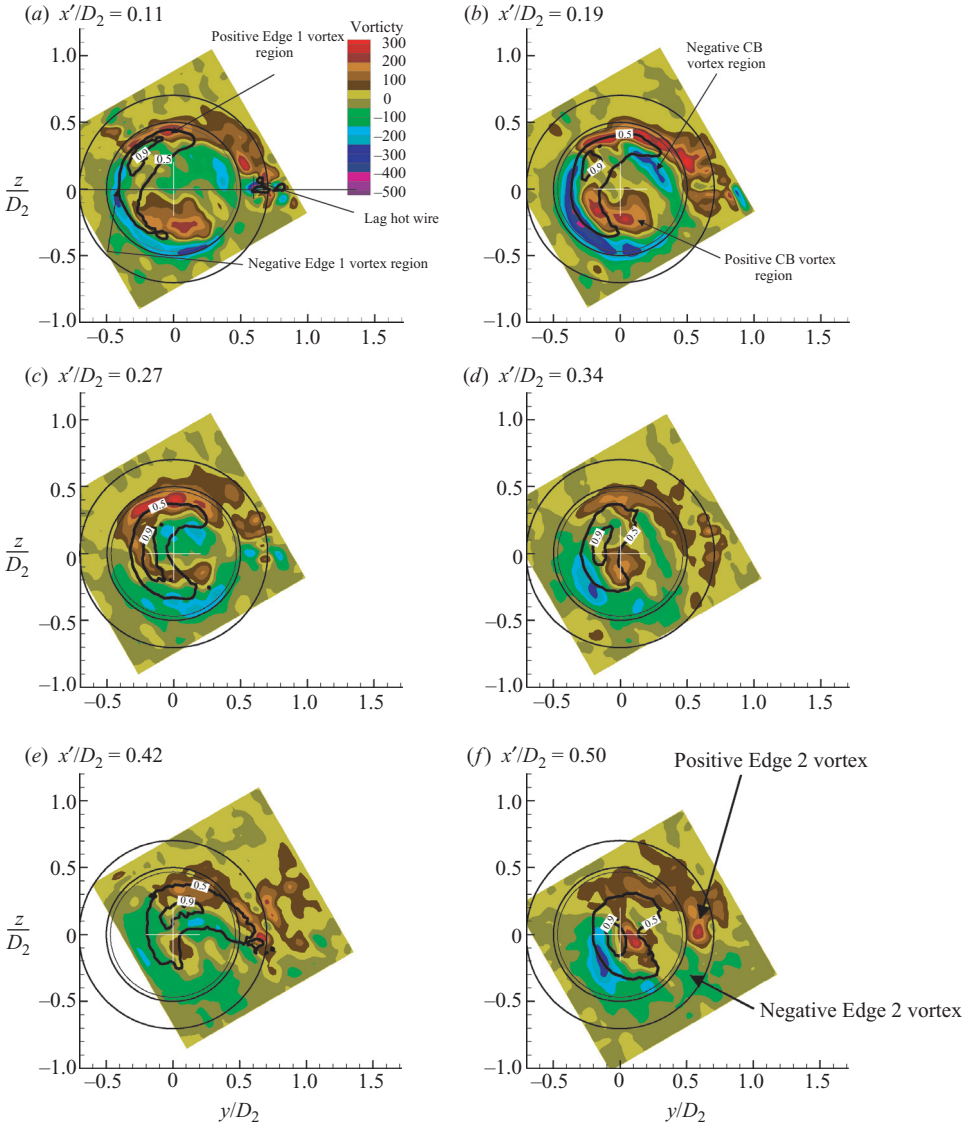

FIGURE 5(*a–f*). For caption see facing page.

flow. The slow response of surface flow-visualization markers, such as china-clay, prevent instantaneous surface flow patterns from being obtained in the precessing flow. Thus, using an assumption that the instantaneous flow pattern of the precessing flow is closely related to that of a steady reattaching jet flow, we biased the jet slightly towards one side of the chamber. This steady flow through the nozzle is analogous to the instantaneous flow and was used to obtain a flow pattern on the centrebody of the FPJ nozzle.

The steady jet that deflects at approximately 45° relative to the nozzle axis was obtained by removing the inlet end of the FPJ nozzle (Ch-L-CB arrangement) and introducing air at an eccentric location in the nozzle inlet plane (figure 2*c*). Air was supplied by diverting a portion of the flow from an open-return open-jet type wind

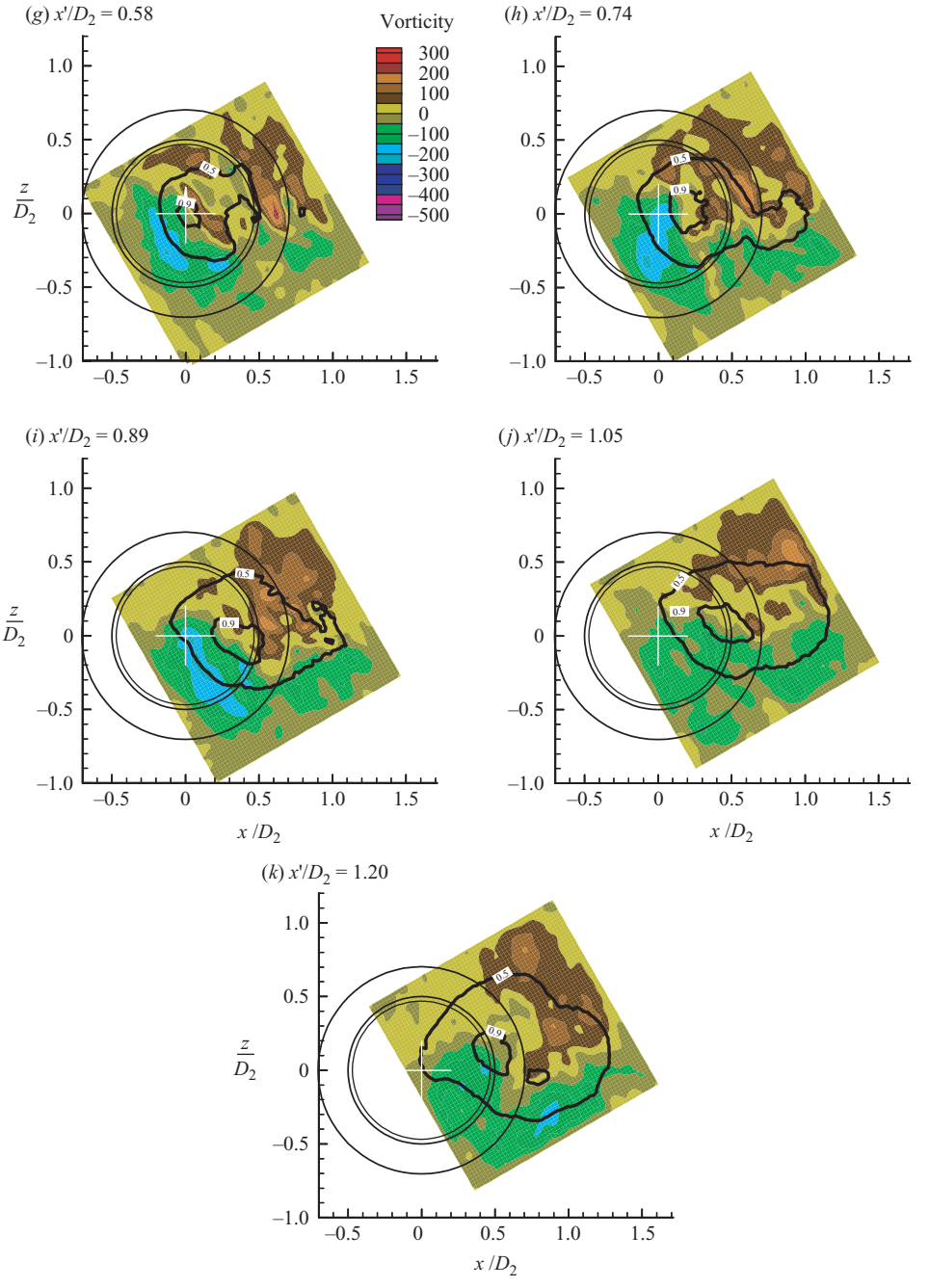

FIGURE 5. Axial vorticity of the phase-direction-triggered PIV in the (y, z)-section when $\eta = 0°$ for $x'/D_2 = 0.11$ to 1.20. Contours representing 0.5 and $0.9(v^2+w^2)^{1/2}_{max}$ are overlaid on coloured axial vorticity contours. Note the qualitative location of Edge 1, Edge 2 and CB vortices and lag hot-wire at $\eta = 30°$. $Re_d = 59000$, $St_d = 0.0017$. The jet is precessing towards the reader in a clockwise fashion. The arrows point to large regions of vorticity which may also contain smaller vorticity 'blobs'.

tunnel (exit area of 0.5 m^2 and tunnel free-stream velocity of 28 $m\,s^{-1}$) using a suitable turning vane. The steadily deflected air-stream emerging from the exit lip was checked with a cotton tuft attached to a stiff metal rod. A mixture of white talcum powder and methylated spirit (96 % ethanol at 20 °C: $\mu = 5.23 \times 10^{-7}\,kg\,m^{-1}\,s^{-1}$, $\rho = 802\,kg\,m^{-3}$) was used for the surface flow-visualization experiments on the matt-black centrebody and exit-lip surfaces.

3. Results

3.1. *Transverse sections*

Figure 4 presents, the various phase-averaged in-plane velocity magnitudes and streamline patterns for 11 downstream measurement planes relative to the FPJ exit lip at $Re_d = 59\,000$. Each phase-averaged pattern represents an ensemble average of 50 images. Phase-averaged measurements represent approximately the instantaneous velocities in many flows (Cantwell & Coles 1983; Hussain & Reynolds 1972). It is the velocity due to the mean flow and the overwhelming unsteady cyclical motion. The series of three concentric circles evident in figure 4, from the innermost to the outermost, respectively, are the centrebody, the edge of the exit lip and the outside edge of the centrebody. These circles are also featured in figures 5 to 8.

The streamline patterns in figure 4 are the projections of the three-dimensional streamline patterns onto each sectional plane. The jet in these figures is precessing in a clockwise fashion relative to an observer looking upstream. The figures indicate that the jet at $x'/D_2 = 0.11$ is initially kidney-shaped (or 'crescent-shaped' as defined in Wong *et al.* 2003), but gradually transforms into a roughly circular jet near to $x'/D_2 = 0.50$. This location is near to the 'flow convergence' region also discussed by Wong *et al.* (2003) who explain that the flow convergence region forms owing to the impact of the kidney-shaped jet flow at the nozzle exit plane converging approximately $0.5D_2$ downstream in the locality of the nozzle centreline. Perry & Chong (1987) pointed out that a major disadvantage in using instantaneous streamline patterns to locate vortical features is the sensitivity of these patterns to the choice of the velocity of the observer and that vortical features may be better represented by a quantity such as vorticity. Nevertheless, the streamline patterns can be expected to provide new qualitative insights into the structure of the flow under investigation, especially near to the centre of the centrebody.

Figure 5 presents the measured axial vorticity field ($\omega_x = \partial v/\partial z - \partial w/\partial y$) of the downstream measurement planes corresponding to the total in-plane velocity measurements presented in figure 4. Overlaid onto this axial vorticity field are $0.5(v^2 + w^2)^{1/2}_{max}$ and $0.9(v^2 + w^2)^{1/2}_{max}$ contours, which indicate the approximate shear-layer boundary and the region of the maximum in-plane velocity $(v^2 + w^2)^{1/2}$, respectively.

There is inevitably some uncertainty in the present technique (in part from the limited sample size) used to identify individual vorticity 'blobs' as their relative positioning and shape in the image plane can vary between the different measurement planes. To mitigate this risk, we analysed the data using two steps. First, we demarcate the main vorticity regions by inspecting the iso-contours (above zero for positive vorticity and below zero for negative vorticity) below each group of 'vorticity blobs' recursively just until all the significant 'blobs' for each region are enveloped within a common vorticity contour. That is, the collective groups of 'vorticity blobs' constitute one 'vorticity region'. Secondly, we performed a spatial low-pass filter of each phase-averaged vorticity field to identify the spatial centre of these blobs within each

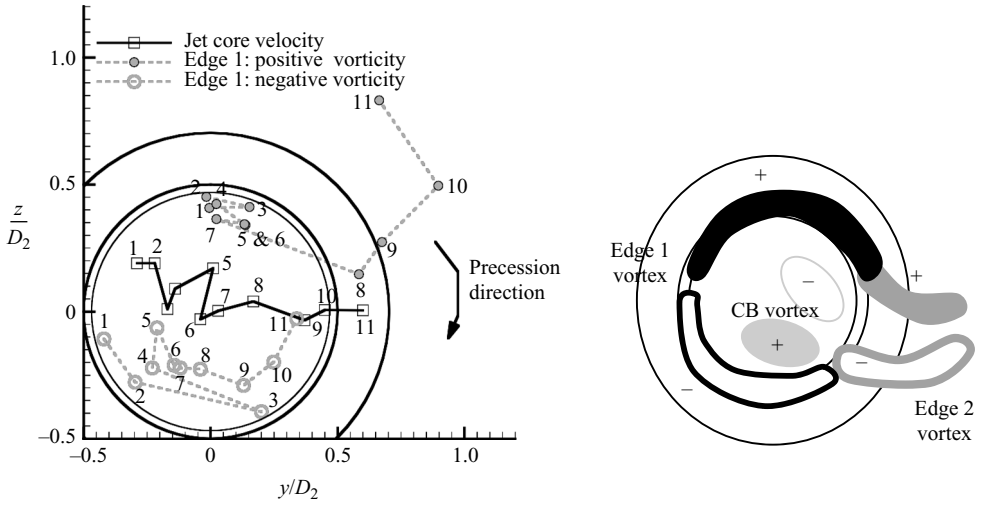

FIGURE 6. Position of weighted vortex centres (circles) and jet core (squares). Numbers 1 to 11 correspond to x'/D_2 {point number} = 0.11{1} , 0.19{2}, 0.27{3}, 0.34{4}, 0.42{5}, 0.50{6}, 0.58{7}, 0.74{8}, 0.89{9}, 1.05{10} and 1.20{11}, respectively. $Re_d = 59000$, $St_d = 0.0017$. Filled symbols are positive vorticity values.

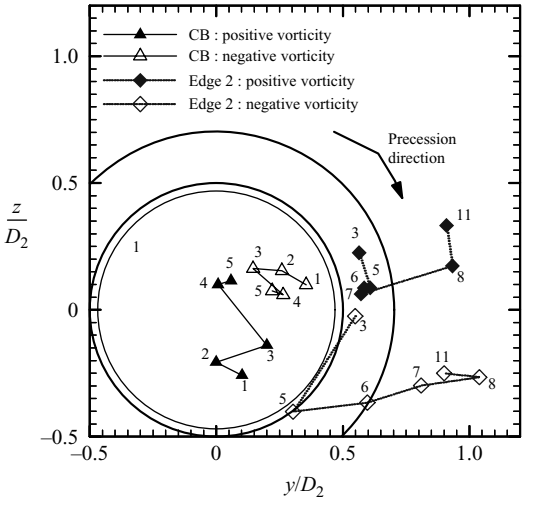

FIGURE 7. Trajectory of the central vortex pairs (CB) and the vortex pairs beyond the edge of the centrebody (Edge 2) for various downstream locations (x'/D_2) based on the estimated location of maximum axial velocity position from axial-radial velocity data in longitudinal sections. Refer to figure 6 for references to numbers. Some of the data are not presented owing to lack of information or because they were not clearly shown in the results. Precession is clockwise. $Re_d = 59000$, $St_d = 0.0017$. Filled symbols are positive vorticity values.

vorticity region. This process smooths out the individual vorticity blobs contained within each vorticity region and provides a method to locate approximately the weighted centres of these larger vorticity regions. This process was repeated for all the phase-averaged vorticity fields. The weighted spatial maximum locations of these vorticity regions are shown schematically as points in figures 6(*a*), 7 and 8(*a*). However, for completeness, the unfiltered data are presented in figure 5.

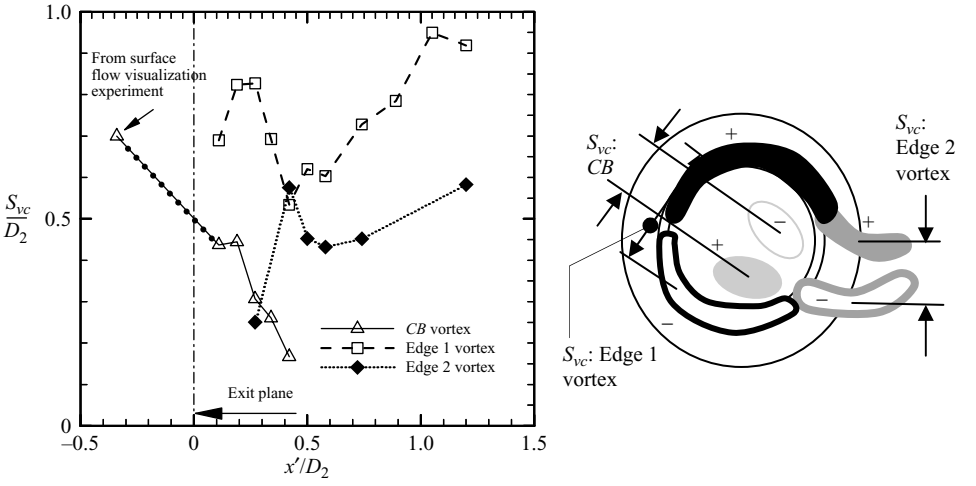

FIGURE 8. Distance between vortex cores, S_{vc} estimated from figures 5 for various downstream distances x'. All data points were measured under precessing jet conditions, except for the point for the CB vortex at $x'/D_2 = -0.34$ which was measured under a steady deflected jet condition. $Re_d = 59000$, $St_d = 0.0017$.

The vorticity fields in figure 5 show that three systems of vorticity regions are present, namely the Edge 1, CB (centrebody) and the Edge 2 vortex regions. It can be seen from figure 5(*a*) that there are large elongated regions of high axial vorticity near to the exit flow. The coherence and persistence of these regions throughout the various cross-sections suggest that these regions are associated with vortices that roll up from the centrebody, or originate from within the cavity. The elongation of the vorticity patches or blobs suggests that these vortices may cut the measurement plane at a large angle to the normal. The vortex pair associated with the location of the maximum in-plane velocity, $(v^2 + w^2)^{1/2}_{x',max}$, at the exit plane is herein referred to as an Edge 1 vortex pair since it emerges with the jet from the interior of the chamber.

Figure 5(*a*) also reveals a pair of high axial vorticity regions near to the downstream face of the centrebody, within the Edge 1 vortex pair. These regions are hereinafter called the CB vortex pair regions. The origin of this feature is described by the surface flow-visualization experiment performed on the downstream face of the centrebody (see § 3.4).

A third pair of vortex regions is also found towards the rear edge of the jet in figure 5. These vortex regions are only clearly identifiable downstream from $x'/D_2 = 0.27$ and are herein called the Edge 2 vortex pair.

Figure 6 presents the jet core locations superimposed onto the trajectory of the jet vortex centres in the (y, z)-plane. The jet core location is taken to be the position of the maximum in-plane radial and tangential velocity $(v^2 + w^2)^{1/2}_{max}$ within each measurement plane. A first-order estimation of the uncertainty in the spatial location of each point can be inferred from the scattering of the data owing to phase-jitter shown in figure 18 taken at $x'/D_2 = 0.11$. The influence of phase-jitter at this position will largely determine the data scatter of the subsequent points downstream of the nozzle exit plane. The uncertainty in detecting the peak magnitude of in-plane velocity in the exit plane is estimated to be approximately $\pm 30°$ for up to 75 % of the recorded samples in the azimuthal direction and $\pm 0.1 D_2$ in the radial direction.

These uncertainties also apply to locating the spatially averaged vorticity maximums in figures 6 to 8.

Figure 6 shows that the direction of the jet core is approximately constant between planes 1 and 9. However, in plane 9 ($x'/D_2 = 0.89$), the jet starts to veer counterclockwise towards the rear, in the direction of the positive Edge 1 axial vorticity, away from the direction of clockwise precession. This phenomenon may be associated with the rearward turning of the positive Edge 1 vortex pair in plane 9. The direction of the jet core beyond plane 9 is relatively unchanged relative to the positive Edge 1 vortex which moves a considerable distance counterclockwise, opposite to the direction of jet precession.

The negative Edge 1 vortex is located in the vicinity of $y/D_2 = -0.2$ and $z/D_2 = -0.4$ until after plane 9 and appears to be associated with the location of the jet core. This is in stark contrast to the positive Edge 1 vortex which appears to stay at $y/D_2 = +0.2$ and $z/D_2 = +0.4$ for most of the downstream measurement planes before $x'/D_2 = 0.74$. In summary, the position of the jet core appears to be closely associated with the Edge 2 vortex pair. However, after plane 9, the rearward motion of the jet core is weakly associated with the positive Edge 1 vortex and is associated with the rapid velocity decay of the jet.

Figure 7 gives the trajectory of the CB vortex pair and that of the Edge 2 vortex pair in the (y, z)-plane. The CB vortex pair appears to originate from the downstream face of the centrebody. The separation distance between the positive and negative CB vortices decreases with downstream distance from the exit plane. They are centred at approximately $y/D_2 = +0.2$ and $z/D_2 = +0.1$. These vortex regions are not detectable beyond $x'/D_2 = 0.50$ (plane 6), suggesting that they annihilate each other when they merge. The Edge 2 vortex regions are detectable at most planes beyond $x'/D_2 = 0.42$ (plane 5). The positive Edge 2 vortex appears to be initially anchored at $y/D_2 = +0.6$ and $z/D_2 = +0.1$, but begins to depart from this anchor location at $x'/D_2 = 0.74$ (point 8). Its negative counterpart seems to be closely associated with the general trajectory of the jet core.

Figure 8 presents the non-dimensionalized linear distance S_{vc}/D_2 between each positive and negative vortex pair as a function of downstream distance x'/D_2 for the CB vortex (open triangles), Edge 1 vortices (open squares) and Edge 2 vortices (closed diamonds). The value of $S_{vc}/D_2 \sim 0.7$ obtained from the surface flow-visualization experiment for a steady deflected jet is also plotted in the figure. The figure shows that the separation distance between the CB vortices decreases steadily until about $x'/D_2 = 0.5$ before the CB vortices become indistinguishable from the other vortices. As explained earlier, the undetectability of these CB vortices beyond this location may be attributed to a mutual annihilation of their opposite vorticities as they converge in the vicinity of $x'/D_2 = 0.50$.

The separation between the respective cores of the Edge 1 and Edge 2 vortex pairs increases initially to a maximum value before decreasing rapidly to a minimum and then increasing again with downstream distance from the exit lip. A similar trend is seen with the Edge 2 vortex pair. The first maximum separations for the Edge 1 and 2 vortices are approximately $S_{vc}/D_2 = 0.5$ and 0.7, respectively. Importantly, at the 'flow convergence' plane, the Edge 1 vortex pair exhibits a minimum separation and the Edge 2 vortex pair exhibits a local maximum separation. Note also that the first detection of the Edge 2 vortex pair does not occur until approximately $x'/D_2 = 0.34$. This coincides with the initial decrease of the separation of the Edge 1 vortex pair. This may suggest that the emergence of the Edge 2 vortex has some influence on the relative spacing between the pair of Edge 1 vortices. By the final measurement plane,

their separation distances are, respectively, $S_{vc}/D_2 = 0.95$ and 0.6 for the Edge 1 and Edge 2 vortex pairs.

Finally, from a comparison of figures 6 and 7, it is shown that the trajectories of the positive Edge 1 vortex and the positive Edge 2 vortex are broadly similar, with the Edge 2 vortex lying generally below (i.e. in a lower axial location than) the Edge 1 vortex. The trajectories of the negative Edge 1 vortex and the negative Edge 2 vortex follow a similar trend, although the trajectories of these vortices tend to be more divergent.

3.2. *Longitudinal sections*

Figure 9 present, the results of the precession-direction-resolved phase-averaged velocity field in the (x', r)-plane for various longitudinal sections of the jet through the FPJ nozzle axis at $Re_d = 59\,000$. Each phase-averaged pattern represents an ensemble average of 50 velocity image pairs. The time delay for this set of experiments was set at $\Delta t = 15\,\mu s$ and the lightsheet thickness was likewise approximately 2 mm at the nozzle axis. The magnification 94 μm pixel^{-1} and an interrogation window of 16×16 pixels with no overlapping samples implies that the actual dimensions of each measurement volume were $1.51 \times 1.51 \times 2$ mm^3. An error-correction technique by the method of Hart (2000) was used to reduce the number of spurious vectors.

Figure 9(f) shows that the bulk jet initially emerges at approximately $\theta = 40^\circ$ relative to the nozzle axis, but the angle decreases to a smaller value ($\theta < 10^\circ$) near to $x'/D_2 = 0.47$. This is consistent with the LDA results in Wong *et al.* (2003) who reported that the bulk jet is turned through a smaller angle relative to the nozzle axis after the 'flow convergence' at that location. However, the transverse sections in figures 4 and 5 demonstrate that the core of the downstream precessing jet actually lags the initial jet core at the exit plane, that is, it is deflected out of the plane of the lightsheet. This 'out-of-plane' motion (relative to the transverse lightsheet in the (y, z)-plane) is observed in some longitudinal cross-sections (e.g. figure 9f, h) corresponding to a reduction in the measured 'core' axial velocity in any one (x', r)-longitudinal section (Wong *et al.* 2002). The region of flow convergence between $x'/D_2 = 0.3$ and 0.7 is also presented more clearly in these longitudinal cross-sections (figure 9) and in figure 16(c).

Nearer to the exit plane at $x'/D_2 = 0.06$, there is evidence of phase-averaged flow reversal in the region downstream from the centrebody ($r/D_2 \sim 0$). There is also evidence of a separation in the region $-0.7 \leqslant r/D_2 \leqslant -0.5$ and $0.5 \leqslant r/D_2 \leqslant 0.7$. The velocity data do not provide details as to the source of the 'reversed' flow in the gap between the exit plane and the centrebody, or of the separated region seen in these velocity fields. More insight into this issue is gained from the surface flow-visualization results presented in § 3.4.

Figure 10 presents the total r.m.s. fluctuating velocity fields for the respective phase-averaged velocity fields in figure 9. The broad features of the r.m.s. fluctuating velocities are similar to the corresponding phase-averaged velocity fields. These measurements of r.m.s. fluctuating velocities are expected to be more representative of the instantaneous flow than previous phase-averaged r.m.s. fluctuating velocity measurements (Wong *et al.* 2003), which were not direction resolved. However, because of the limited sample size (nominally 50 image pairs) and relatively poor spatial resolution of the present experiments, higher-order statistics calculated from the data would not be reliable and are not presented.

Figure 11 presents the azimuthal two-dimensional vorticity fields for the respective phase-averaged velocity fields shown in figure 9. These results give evidence to

complement some of the observations reported in the (y, z)-cross-sections in figure 5, and will assist in the interpretation of the flow topology of this jet in § 4.

3.3. *Centreline velocity of the phase-averaged jet*

Figure 12 summarizes the magnitudes of downstream velocity obtained from all the phase-averaged data discussed in §§ 3.1 and 3.2, and compares them with the data of Crow & Champagne (1971) for an unforced free turbulent jet produced by a smoothly contracting round nozzle at $Re_d = 83\,000$ and also with phase-averaged axial velocity data from an analogous mechanical precessing jet (Schneider *et al.* 1997*b*). Measurements of the local jet are obtained along the local jet axis, x'_{jet} (figure 2) from several longitudinal planes, neglecting the out-of-plane component of velocity. Compared with a free turbulent jet, the local FPJ centreline velocity decays very rapidly from a maximum $(u^2 + v^2)^{1/2}_{e,max}$ at the exit plane to $0.6(u^2 + v^2)^{1/2}_e$ by $x'/d = 2.34$ ($x'/D_2 = 0.58$ or $x'_{jet}/d = 2.74$). Here, $(u^2 + v^2)^{1/2}_e$ represents the maximum total magnitude of the axial (u) and radial (v) velocity component in the longitudinal plane ((x', r)-plane), where the subscript 'e' indicates measurements at the FPJ jet exit plane. The velocity decay beyond $x'/d = 2.34$ is less rapid and follows a similar trend in decay rate to that of the MPJ, that is, a rapid initial rate of decay followed by a more gradual rate of decay. Note that this comparison is sensitive to the definition of 'd'. In the present calculation, 'd' represents the diameter of the jet at the FPJ inlet plane, $d = 15.79$ mm.

The initial deflections of the jet core about a mean trajectory, represented as open squares in figure 6, coincides with the commencement of the rapid decay of the emerging jet in figure 12. The rapid deflection later at $x'/D_2 = 0.89$ (plane 9 in figure 6) coincides with the slower decay rate beyond that point.

3.4. *Surface flow patterns on the FPJ centrebody*

The results of the surface flow-visualization studies on the downstream face of the centrebody for a steady deflected FP jet are presented in figures 13*c* to 15. For the purposes of comparison, two other isolated disks of different diameter-to-thickness ratios were also tested and the results of the flow visualization on their leeward faces are shown in figure 13(a, b). Figure 13(c) shows the centrebody (CB) used in the FPJ nozzle shown in figure 2. It has a centrebody diameter-to-thickness ratio, d_{cb}/t_{cb}, of 3.6. The other disks have ratios of $d_{cb}/t_{cb} = 120$ and 4.5, respectively. Each of these three disks was positioned at the exit plane of an open-return wind tunnel at an angle of attack of approximately 45° relative to the wind tunnel exit centreline. A nominal Reynolds numbers of $Re_{d_{cb}} = 1 \times 10^5$ was used for all the experiments. The surface flow-visualization results for the case of the steady deflected FP jet are shown in figure 14. In this case, the centrebody was installed in the nozzle, and the jet within the FPJ nozzle cavity was deflected as described in § 2.2 with an estimated Reynolds number (based on d_{cb}) of 60 000.

The surface flow-visualization results are interpreted in the light of the assumptions and rules associated with surface flow topology for three-dimensional separated flows described by Perry & Chong (1987); Tobak & Peake (1979, 1982) and Wang (1997). Rockwell (2000) reviewed these concepts in the light of particle-image velocimetry measurements.

Surface flow visualization assumes that the powdered particles in the liquid–powder mixture follow the flow into a persistent pattern over a period of time and that the mean displacement of the particles in the mixture is locally parallel to the mean velocity vector of the air particle just above the surface (Hunt *et al.* 1978).

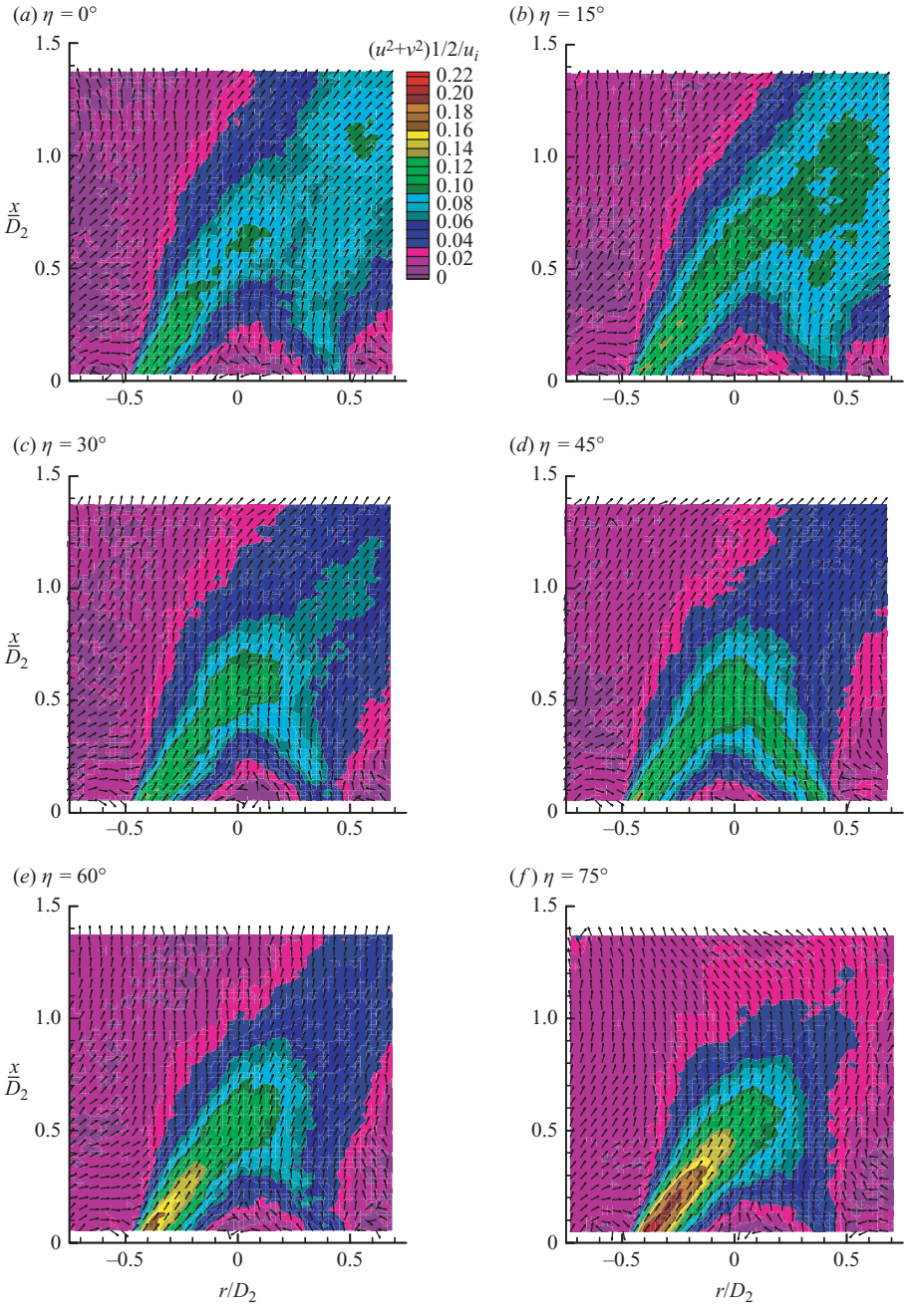

FIGURE 9(*a–f*). For caption see facing page.

Tobak & Peake (1979) maintained that 'the oil-streak flow visualization surface patterns were best interpreted as being representative of skin-friction lines'. If the patterns are interpreted as skin-friction lines, corresponding to a continuous velocity field, certain topological rules can be applied to a limited number of singular points observed on the surface of the object (Tobak & Peake 1979). This implies that only

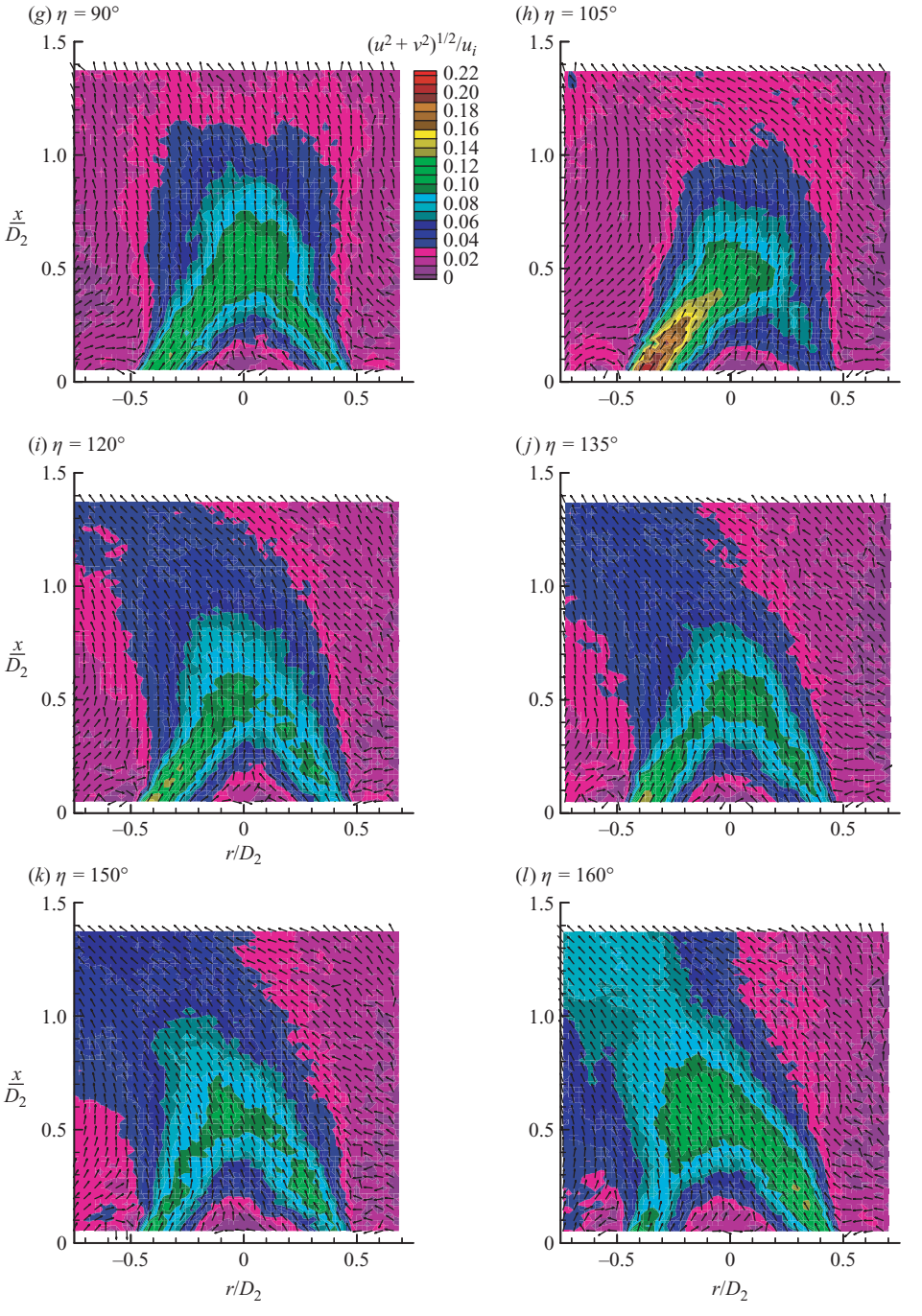

FIGURE 9. Phase-direction-triggered PIV in (x', r) (longitudinal)-section for $\eta = 0°$ to 160°. Coloured contours are normalized velocity magnitude, while arrows show direction of vectors. $u_i = 55.0\,\mathrm{m\,s^{-1}}$ $Re_d = 59\,000$, $St_d = 0.0017$.

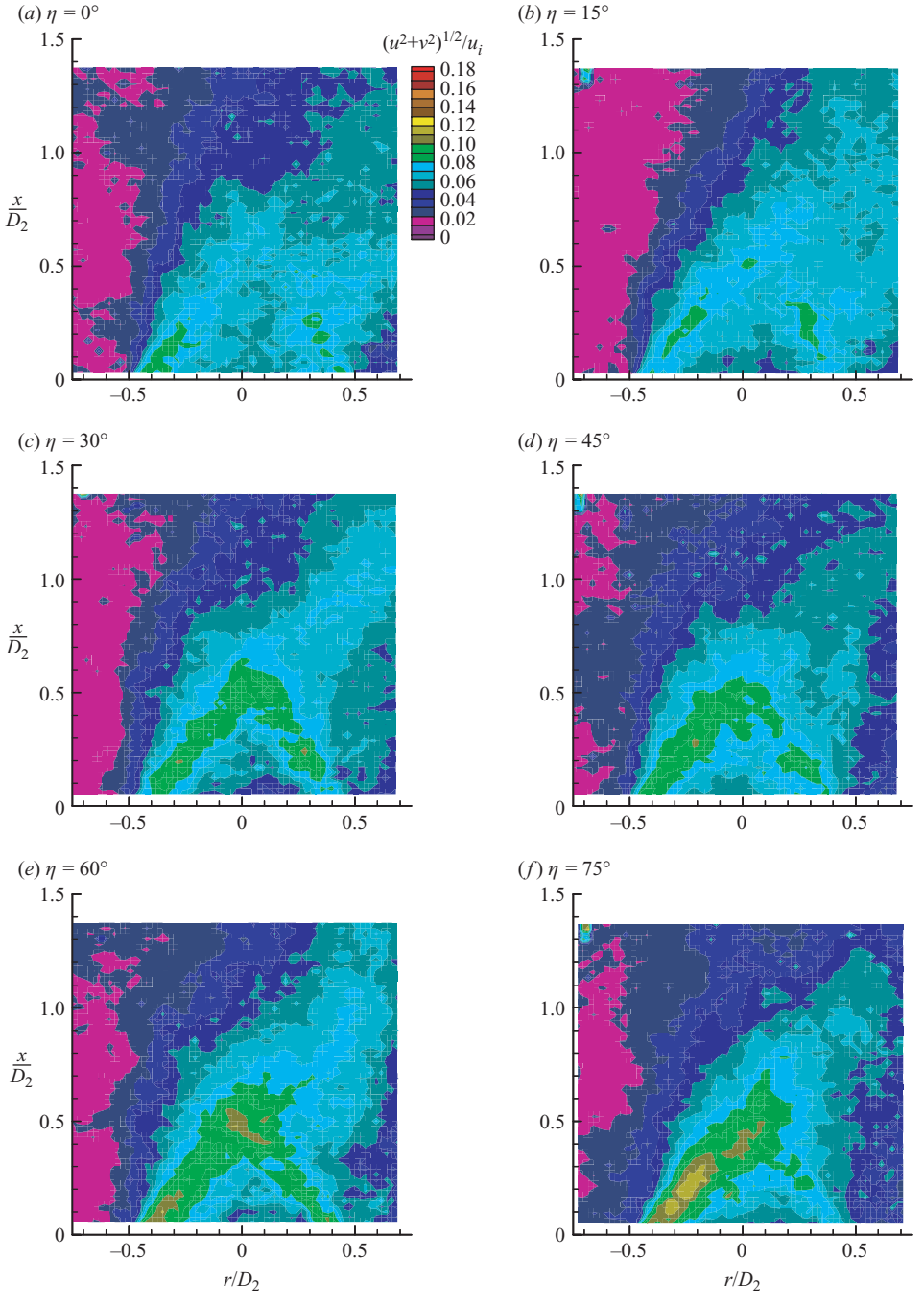

FIGURE 10(*a*–*f*). For caption see facing page.

a limited number of solutions are possible for a flow with a particular boundary condition.

The general features of the leeward surface flow patterns on the centrebody installed in the FPJ nozzle (figure 14, upper right hand corner) are similar to those in the free stream (figure 13*a*). These patterns are also broadly similar to those found on

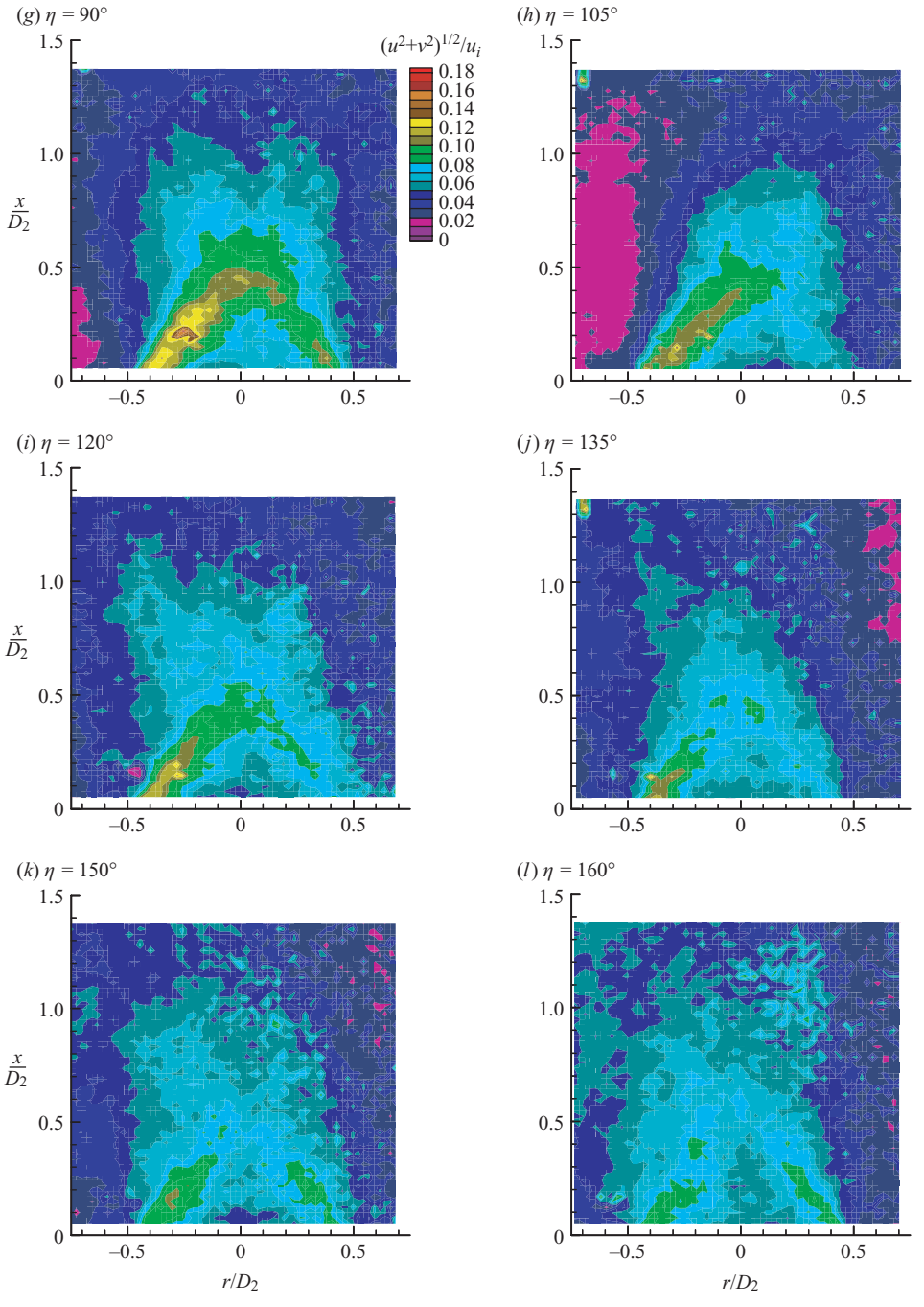

FIGURE 10. Phase-direction-triggered PIV in (x', r) (longitudinal)-section for $\eta = 0°$ to 160°. Coloured contours are normalized r.m.s. velocity magnitude. $u_i = 55.0\,\mathrm{m\,s^{-1}}$, $Re_d = 59\,000$, $St_d = 0.0017$.

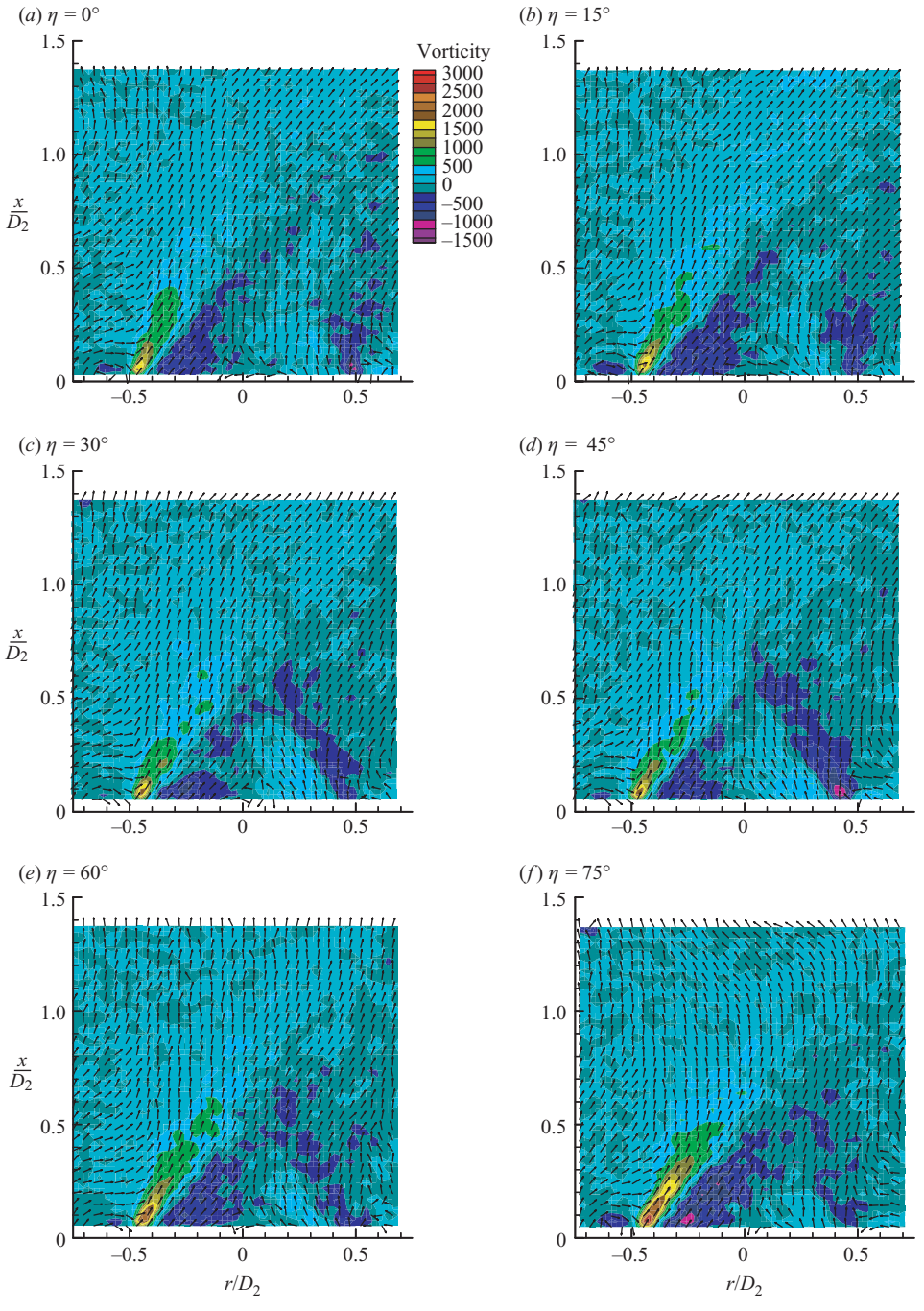

FIGURE 11(*a–f*). For caption see facing page.

the leeward surfaces of a disk by Calvert (1967) and a disk-wing, or a 'Frisbee' (Nakamura & Fukamachi 1991; Potts & Crowther 2000) both inclined at an angle to a free stream, and a coin-like cylinder (Zdravkovich *et al.* 1998) parallel to the free stream.

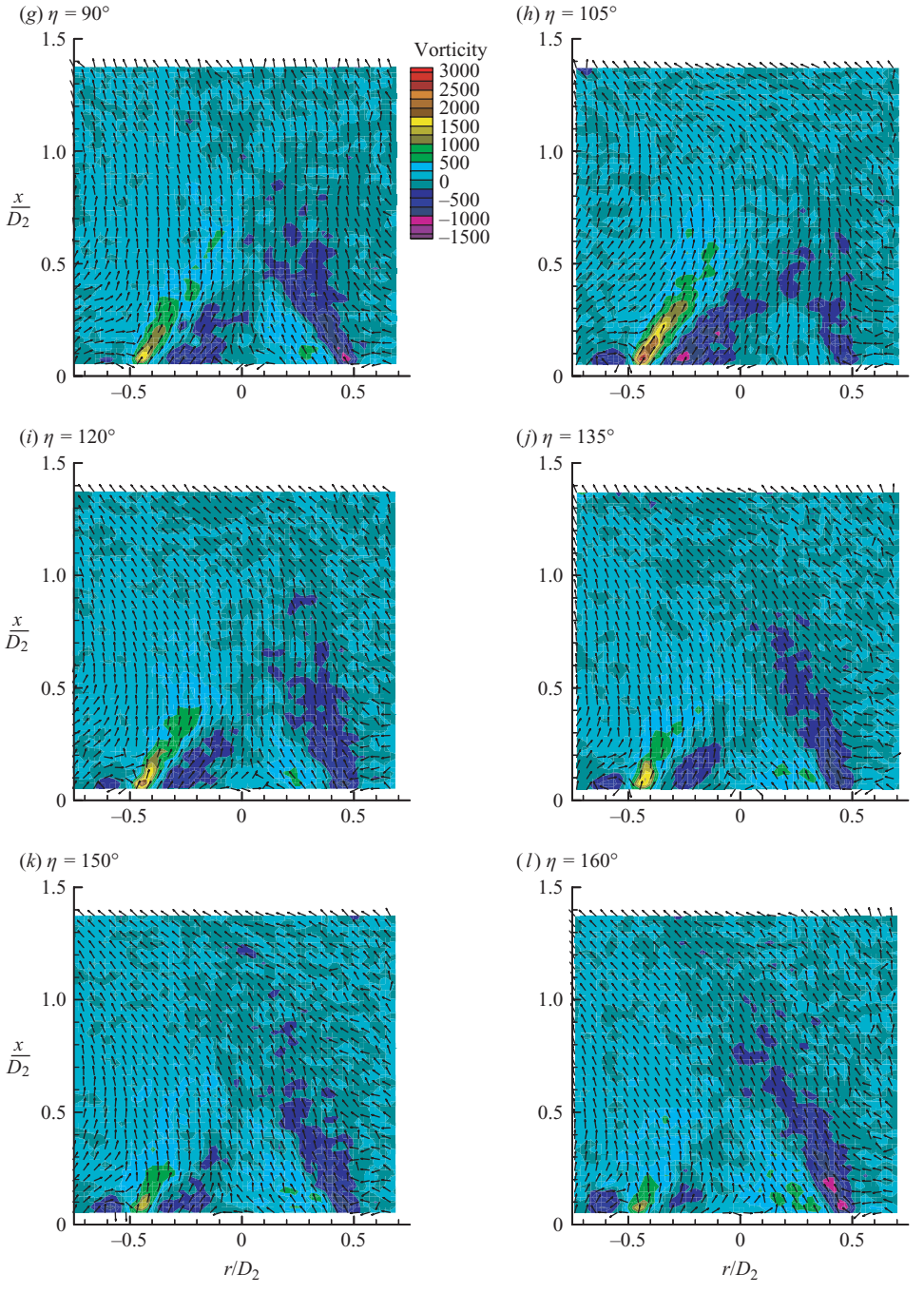

FIGURE 11. Phase-direction-triggered PIV in (x', r) (longitudinal)-section for $\eta = 0°$ to 160°. Coloured vorticity values overlaid onto vectors (only direction) are shown. $Re_d = 59\,000$, $St_d = 0.0017$, $u_i = 55.0\,\mathrm{m\,s^{-1}}$.

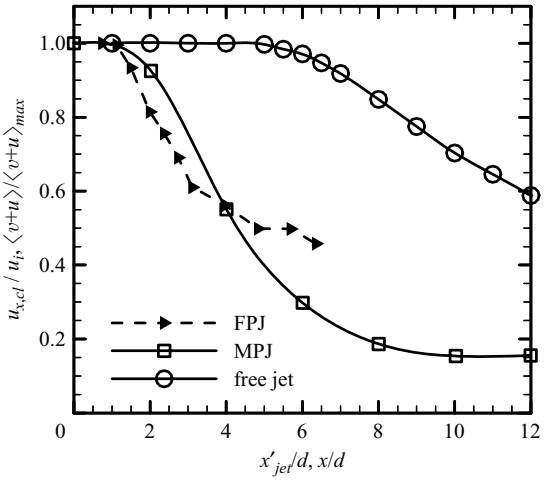

FIGURE 12. Total velocity decay magnitude, $\langle u + v\rangle$, of FPJ at $Re_d = 59\,000$, $St_d = 0.0017$ compared with an MPJ at $Re_d = 26\,000$ (Schneider *et al.* 1997*b*) and a free turbulent jet at $Re_d = 83\,000$ (Crow & Champagne 1971). $\langle u + v\rangle$ refers to FPJ velocity magnitude data $(u^2 + v^2)^{1/2}$ obtained from figure 9, and are normalized with $\langle u + v\rangle_{max} = (u^2 + v^2)^{1/2}_{e,max} = 10.8\,\mathrm{m\,s^{-1}}$ at $x'/D_2 = 0.11$. $u_{x,cl}/u_i$ and x/d refer to normalized axial velocity and axial position, respectively, for MPJ and free turbulent jet. For the FPJ, note that x'_{jet} is normalized by $d = 15.79$ mm.

The main surface features identified on the centrebody are:

(*a*) a primary line of separation;

(*b*) a line of reattachment;

(*c*) a secondary line of separation;

(*d*) a primary stagnation point (half node) further downstream from the secondary separation line;

(*e*) two foci to the left- and right-hand side of the secondary stagnation point; and

(*f*) some evidence of saddle points associated with the foci.

The lines of primary and secondary separations, and the line of reattachment are qualitatively similar to the flow visualization studies by Zdravkovich *et al.* (1998) who performed their experiments for $d_{cb}/t_{cb} = 1.33$, 2.56 and 9.1 at $Re_{d_{cb}} = 2.14 \times 10^5$ in coin-like cylinders.

These features are interpreted in figure 14 which presents the flow pattern on the downstream surface of the centrebody for a steady deflected jet from the FPJ nozzle. The flow pattern shown has the jet inside of the chamber deflected towards the left-hand side of the chamber. This jet exits from the left-hand side around the centrebody and is deflected across the nozzle exit towards the right-hand side. The flow pattern shows that most of the flow emerges from the left-hand side, but some flow exits from around the entire perimeter of the centrebody, as shown by Wong *et al.* (2003). Furthermore, the flow visualization shows a pair of separation lines on the downstream face of the centrebody connected to a pair of focal points (F and F'). These suggest that a pair of vortices originates from the downstream side of the centrebody. A node of attachment (N) is also apparent on the top of the centrebody. This corresponds to a point where the jet flow splits, with some jet fluid being turned towards the primary and secondary separation lines. From the pattern of separation and attachment lines, it is apparent that a system of vortices is present

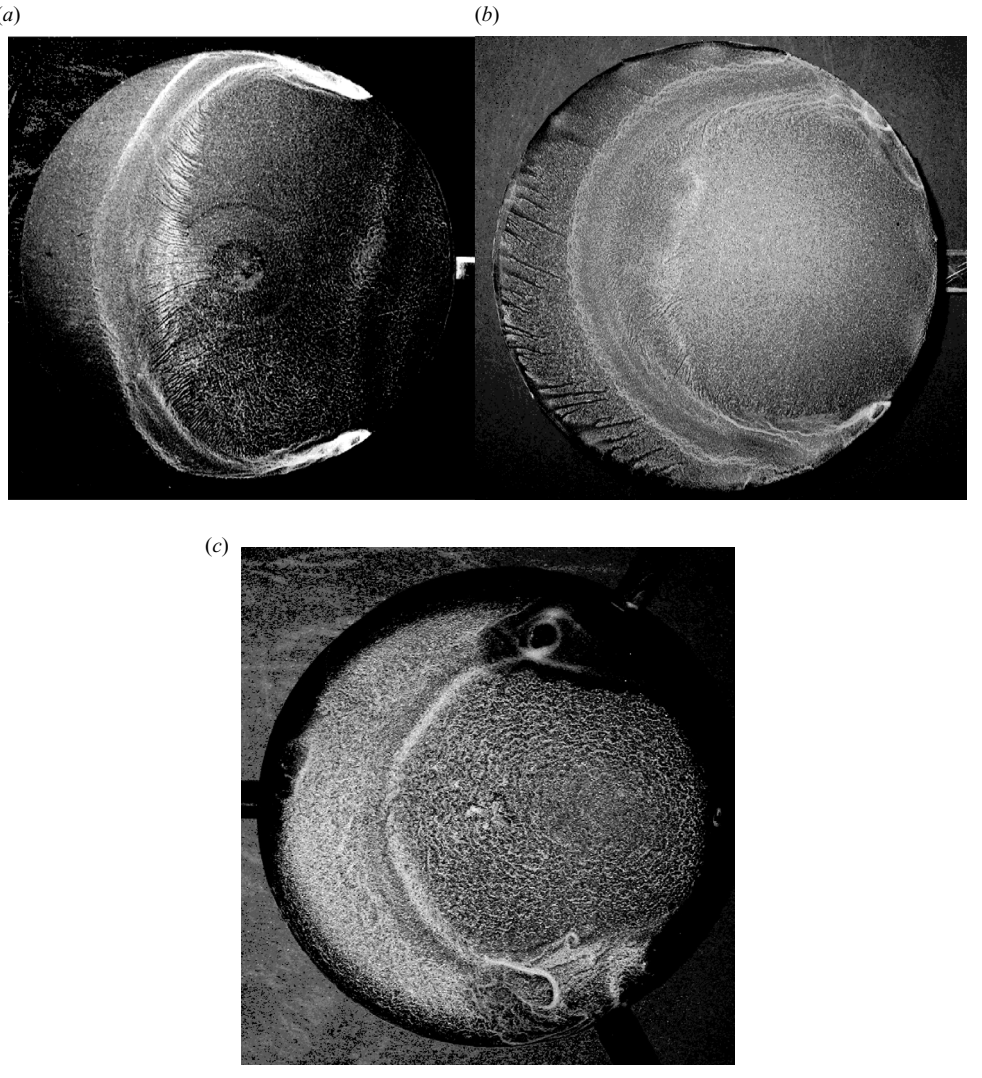

FIGURE 13. Effect of varying d_{cb}/t_{cb} – surface flow visualization on the leeward surface of (*a*) a thin disk ($d_{cb}/t_{cb} = 120$, $d_{cb} = 0.12$ m, $Re_{d_{cb}} = 1.1 \times 10^5$) (*b*) a thick disk ($d_{cb}/t_{cb} = 4.5$, $d_{cb} = 0.10$ m, $Re_{d_{cb}} = 0.9 \times 10^5$ and (*c*) the FPJ centrebody along with the supports ($d_{cb}/t_{cb} = 3.6$, $d_{cb} = 0.6$ m, $Re_{d_{cb}} = 0.4 \times 40^5$). All test objects were inclined at an angle of attack of 45° to the free stream flowing from left to right.

immediately downstream from the centrebody surface, similar to those observed by Potts & Crowther (2000). Further evidence of the flow complexity was found after the FPJ nozzle was disassembled and a pair of foci (see figure 14, bottom right) was observed on the edge of the centrebody. These foci are connected with the saddle features on the downstream surface of the centrebody as shown in figure 14. For instance, the saddle '*S*' in the plan view is connected to the rear-focus (F_R).

The accumulation of flow-visualization particles into a line on the surface of the exit lip also suggests the presence of flow bifurcation (see Perry & Chong 1987). Figure 14 therefore indicates that at least two vortices exist above the lip surface.

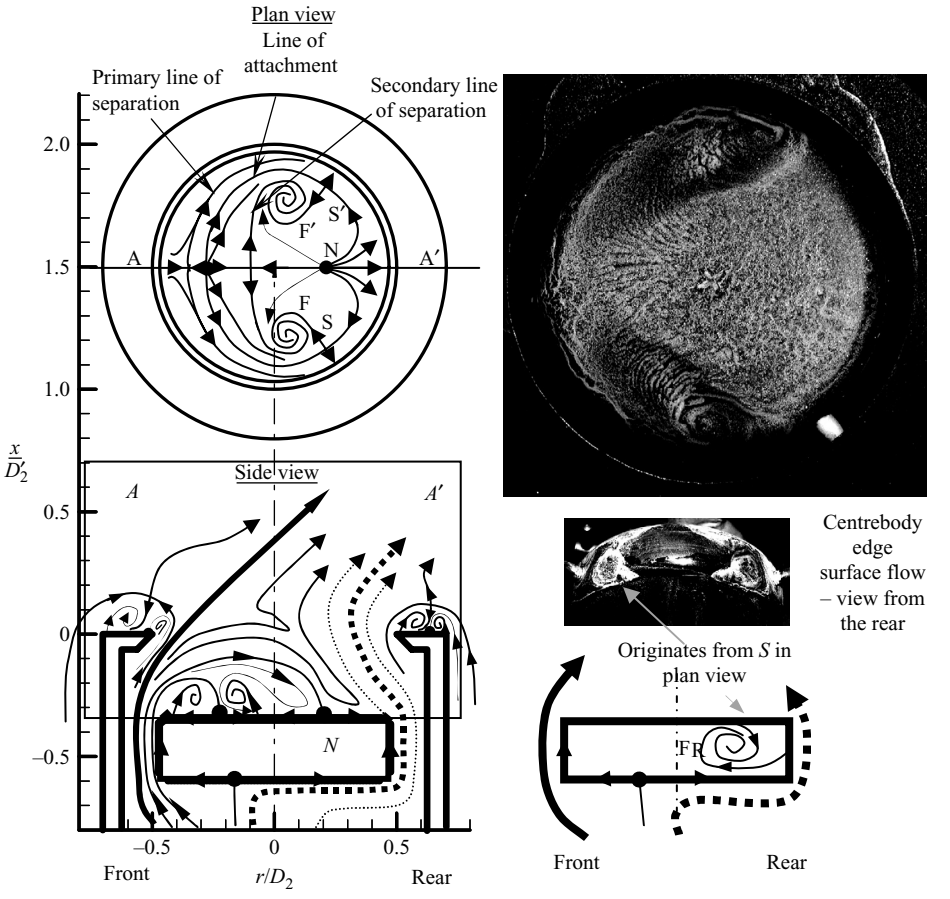

FIGURE 14. Interpretation of surface flow visualization results. Here S and S' represent saddles, F, F' and F_R are foci, and N is a node of attachment in the surface flow. Mean flow direction, from left to right, is indicated by the boldest arrow in the side view. Node of attachment, N, is approximately $0.19D_2$ from the centrebody centre. Some features in section A–A' are shown in figure 16. $Re_d \sim 32\,000$, $St_d = 0$, $u_i \sim 30$ m s^{-1}.

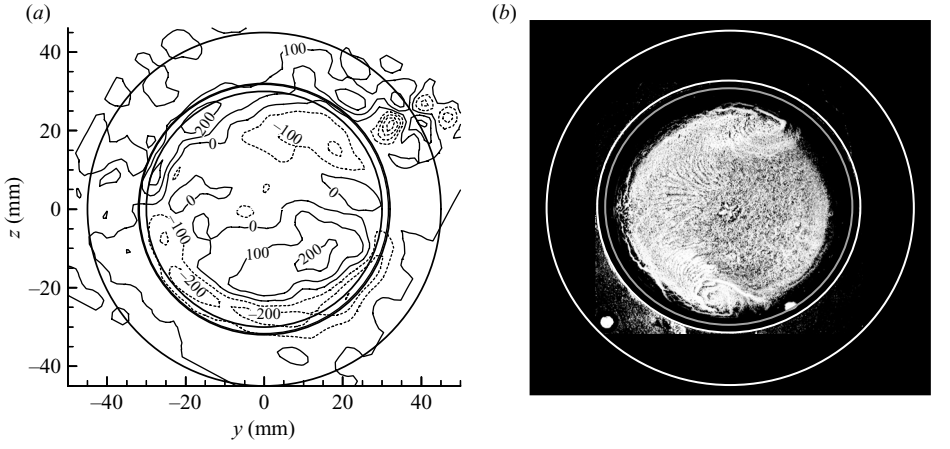

FIGURE 15. Direct comparison of (*a*) vorticity field slightly downstream ($x'/D_2 = 0.11$, $Re_d = 59\,000$, $St_d = 0.0017$) from the (*b*)centrebody surface ($x'/D_2 = -0.34$, $Re_d \sim 49\,000$, $St_d = 0$), with the observer looking upstream. Flow is emerging from left to right.

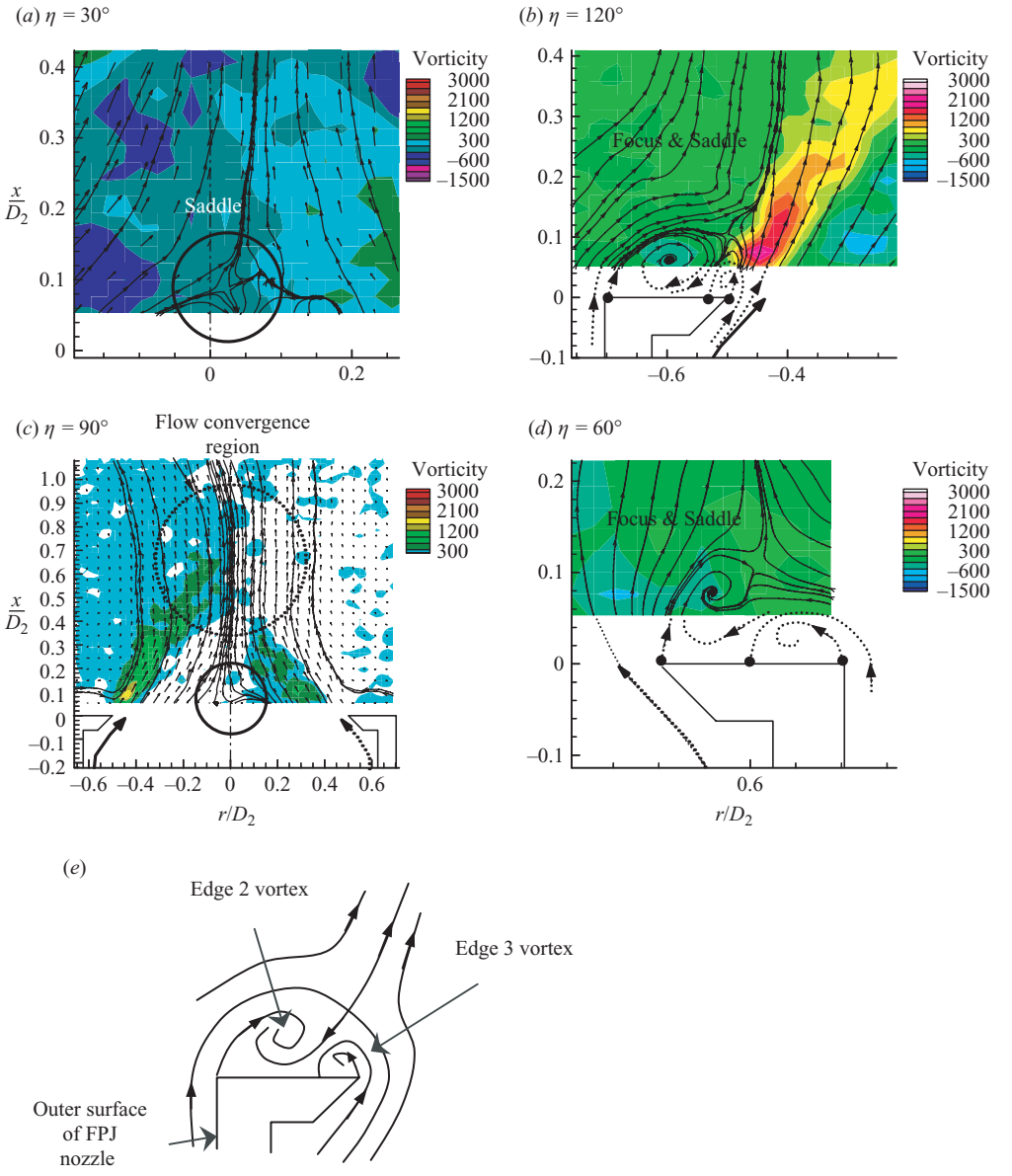

FIGURE 16. Selected topological features identified from figure 11. All conjectured streamlines are shown as dotted lines. (*a*) Saddle point located at $x'/D_2 \sim 0.1$ (*b*) Focus–Saddle pattern at the exit lip with the head of the focus facing inwards. (*c*) Positive azimuthal vorticity contours in which the flow-convergence region is highlighted (circled dotted lines). Also note that the streamline patterns near to $x'/D_2 \sim 0.1$ and $r/D_2 = 0$ (circled solid lines) are interpreted in figure 14. Negative vorticity contours are not shown for contrast; (*d*) Another focus-saddle pattern at the exit lip with the head of the focus facing outwards. Proposed streamlines are shown as dotted lines. (*e*) Proposed streamline patterns for (*b*) $\eta = 120°$ describing the Edge 2 and Edge 3 vortices. $Re_d = 59\,000$, $St_d = 0.0017$.

Further evidence for these vortices is discussed in § 4 and is shown in the PIV results in figures 16*b* and 16*d*.

The experiments show that a series of vortices are generated by the steady deflected jet. The largest of these structures appears to originate from the foci

on the downstream face of the centrebody. Because the surface flow patterns were produced by a statically deflected jet, some details of this pattern will inevitably differ from that of the instantaneously precessing jet. However, key features of the geometric configuration are sufficiently similar for the flows to be analogous. The insight gained from this analogous, albeit simplified, flow is found to be a valuable aid in interpreting the more complex precessing flow. As such, it is deduced that the steady features found in the statically deflected jet are also present in the unsteady precessing flow. Figure 15 further demonstrates that the results obtained from the phase-averaged PIV results are consistent with the results of the surface flow-visualization experiment. The evidence suggests a strong correspondence between the physical location and direction of circulation of the vortical features shown in the surface flow visualization at $x'/D_2 = -0.34$ and the axial vorticity distribution at $x'/D_2 = 0.11$.

4. Discussion of the external structure

Figure 16 summarizes the important structural flow features that can be identified in the longitudinal PIV results from figures 9 to 15. These are,

a saddle (figure 16*a*) above a reversed flow region near to the exit plane in the central region of the nozzle;

a region of separation on the surface of the exit lip whereby the head of the focus points inwards (figure 16*b*);

the mean extent of the flow convergence region (figure 16*c*);

a region of separation on the surface of the exit lip where the head of the focus points outwards (figure 16*d*); and

a conjectured streamline pattern describing the structure of the Edge 2 and Edge 3 vortices (figure 16*e*).

In figure 16(*b*, *d*) some parts of the pattern have been inferred. Note the high positive vorticity concentration at $x'/D_2 = 0.08$ and $r/D_2 = -0.45$. This feature is typical of most of the cross-sections of figure 11. It represents the azimuthal vorticity generated between the exiting jet and the lip. The rounded appearance of the vorticity contours (near to the measurement edges) is an effect of the edge of the velocity measurement grid. The negative vorticity to the right of the exiting jet ($x'/D_2 = 0.1$, $r/D_2 = -0.25$) is consistent with the vorticity generated on the centrebody and is compatible with the presence of the Edge 1 vortex. From these and other transverse cross-section phase-averaged PIV results, a three-dimensional flow topology is proposed for the external precessing jet.

Figure 17 presents a schematic diagram of the proposed flow topology of the precessing jet. Section A–A' in figure 17 is shown by the pattern in figure 14. The thickest solid line with a leading arrow in figure 17(*a*) shows the core of the high-velocity flow, while thick dotted line represents the lower-velocity flow from the nozzle. The thinner lines refer to lines of maximum vorticity associated with the cores of the spatially averaged vortex regions in the flow. The sign (direction of circulation) of each vortex core is indicated by closed ellipses with direction arrows. Positive circulation of a vortex core is defined in a counterclockwise sense for an observer looking upstream, and vice versa for negative circulation.

The pair of thin dash-dot-dashed lines originating from the middle downstream surface of the centrebody (shaded) represents the CB vortex pair. The pair originates from the foci, located on either side of the centrebody surface, as presented in figure 14. Based on figures 6 to 8, these vortices move closer to each other with downstream

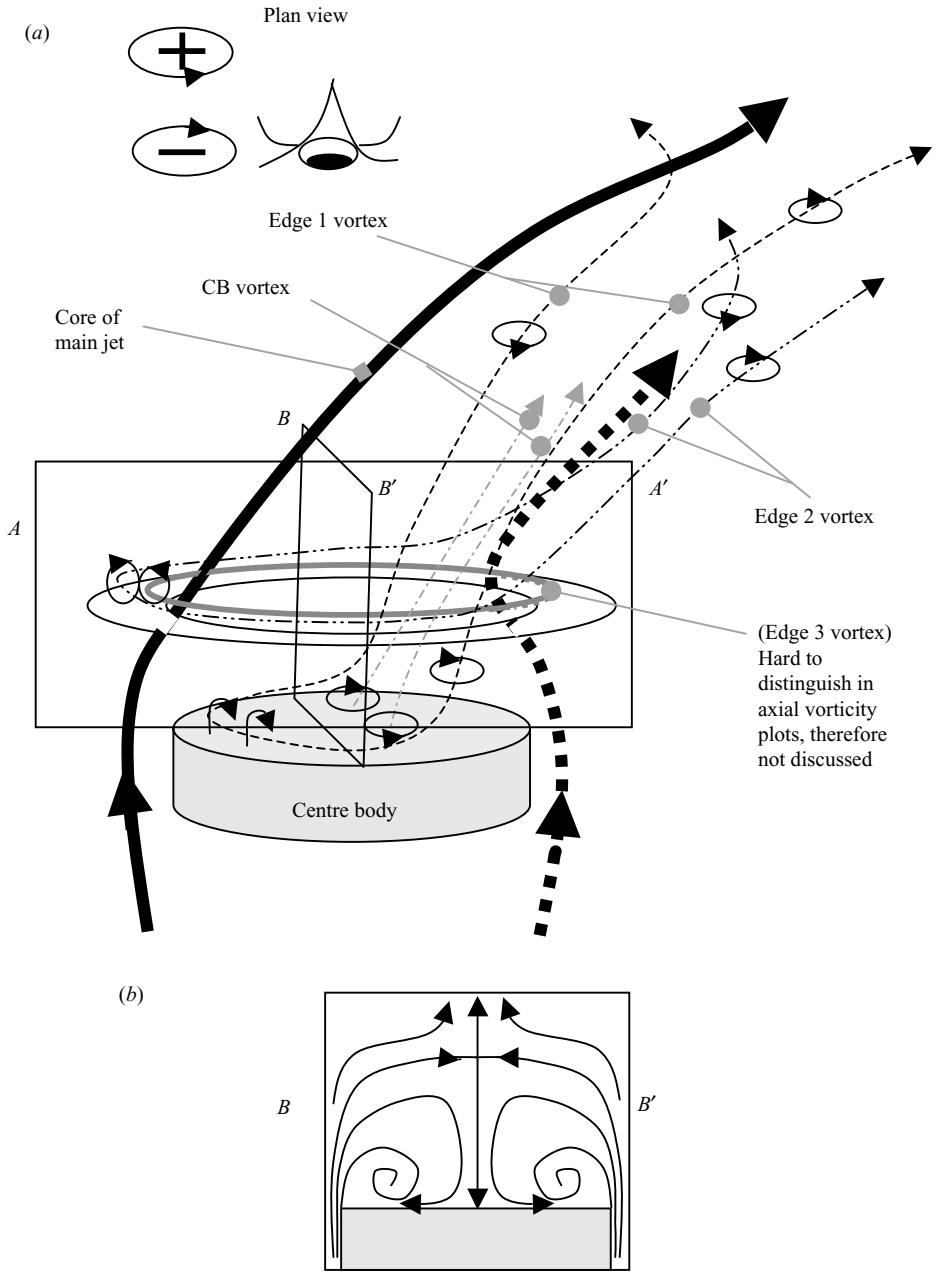

FIGURE 17. (*a*) Proposed flow topology of the external FPJ flow based on instantaneous PIV, phase-and-precession-direction-resolved phase-averaged PIV and surface flow visualization. Interpretation of more details through section A–A' are presented in figure 14. Precession direction is clockwise based on an observer looking upstream. (*b*) Side view of the flow through section B–B' (see figure 16*a*). Diagrams are not to scale.

distance and appear to annihilate one another by $x'/D_2 \sim 0.5$. The thin dashed line represents the vortex that is thought to originate from the edge of the centrebody (that is, the Edge 1 vortex). The 'legs' of this vortex form a pair of longitudinal

vortices downstream from the centrebody (the Edge 1 vortex pair). These appear as positive and negative vorticity regions as seen by a downstream observer. This vortex pair departs from the centrebody at an inclined angle, cutting the lower measurement planes at a large angle. Thus, the vortex pair appears as two kidney-shaped patterns near to the leading edge of the high-velocity jet stream as seen in the transverse PIV measurements of axial vorticity (figure 5). From the evidence presented in figures 6 and 8, the negative leg of this Edge 1 vortex follows the trajectory of the jet fairly closely. The positive Edge 1 vortex is initially located in the vicinity of $y/D_2 = +0.1$ and $z/D_2 = +0.4$, but at a distance $x'/D_2 = 0.58$ (plane 7) it moves towards $y/D_2 = +0.6$ and $z/D_2 = +0.15$ with increasing radius from the nozzle axis while departing in a direction opposite to the jet precession.

The thin dash-dot-dot line, representing the Edge 2 vortex that sits above the surface of the exit lip in figure 22, lifts away from the exit at the rear side of the exiting jet (opposite to the side from which the jet emerges). The lift-off occurs at an angle of 130° to 150° from the centre of the emerging jet. The vorticity associated with this vortex pair is observed most clearly in the longitudinal phase-averaged PIV experiments provided in figure 11. The emerging jet separates at the exit lip to form a saddle-focus pattern at $r/D_2 = -0.6$ at $x'/D_2 = +0.05$ as illustrated in figure 16*b*. This pattern appears to be generated by the separation of the external flow entrained along the outside surface of the FPJ nozzle, and the separation of the exiting FPJ flow at the edge of the lip. The focus seen in figure 16*b* has a direction of circulation (clockwise) that is consistent with the direction of circulation at the outer surface of the FPJ. The focus presented in figure 16*d* is consistent with vorticity shed from the inside of the lip.

Figure 16(*e*) provides one interpretation of these exit lip flow patterns. The pattern is based on the streamlines presented in figure 16(*e*), and also the assumption that the sharp corners and edges of the nozzle are likely to lead to boundary-layer separations. The pattern is also topologically consistent with the streamline pattern presented in figure 16(*d*), although the size, arrangement and orientation of the features are different. The pattern given in figure 16(*e*) is indicated in all the patterns of figure 11 except for $\eta = 15°$ (right-hand side), $\eta = 30°$ (right-hand side) and $\eta = 60°$ (right-hand side) (see also figure 16*d*). The anticlockwise vortex shown below the Edge 2 vortex in figure 16(*e*) is likely to be a relatively small-flow feature. This vortex is denoted as the 'Edge 3 vortex' and is shown by the thicker solid line in figure 17(*a*). The anticlockwise vortex presented in figure 16(*d*) is probably the Edge 3 vortex. If the Edge 3 vortex exists, it will be difficult to distinguish from the vorticity plots of figure 11 owing to its small size and the lack of data close to the nozzle exit. Therefore its presence is ignored in the remainder of the discussion.

It is apparent from figure 16(*b*) and the conjectured topology of figure 17 that the Edge 1 vortex and the Edge 2 vortices are of the same sign of circulation. If the emerging jet were to depart along the geometric axis (i.e. without deflection), then the Edge 2 vortex should remain in a closed 'circular' loop (or ring) sitting above the exit lip. However, the asymmetry of the emerging jet causes one end of this vortex loop to be entrained into the main flow between approximately 130° and 150° ahead of the advancing jet, as provided in figures 5 and 7. This range of angles is similar to the separation angles of the surface flows in jets in crossflow (see Fric & Roshko 1994; Kelso, Lim & Perry 1996). Thus the edge vortex forms a horseshoe-shaped loop with either side of the loop being entrained into the advancing and receding sides of the jet. The trajectories of the two 'legs' of the Edge 2 vortex follow the same trend as the Edge 1 vortex, in terms of the (y, z)-trajectory with downstream

distance, albeit with a slight delay in phase. The presence of the Edge 2 vortex pair below the core of the jet was detected in earlier phase-averaged LDA studies (figure 11C in Wong *et al.* 2003) and in the $0.5(v^2 + w^2)^{1/2}_{max}$ velocity contours of the phase-and-precession-direction-resolved PIV studies (see figures 5). This vortex pair may hold some similarity to the horseshoe vortices (Kelso *et al.* 1996) found in jets in crossflow.

5. Summary

The phase-averaged structure of an external precessing jet is revealed, for the first time, by means of a novel PIV experimental technique that allows the phase and direction of the naturally precessing jet to be resolved. Measurements in both transverse and longitudinal planes of the nozzle centreline were performed up to 1.2 and 1.4 lip diameters, respectively, downstream from the nozzle exit plane. The study found that at least three large-scale fluid vortex pair regions containing several smaller vortical patches exist in this flow:

(*a*) a 'centrebody' vortex pair region that originates from the foci on the downstream face of the centrebody;

(*b*) an 'Edge 1' vortex pair region surrounding the inner 'CB vortex pair' region and likely to originate from the edge of the centrebody; and

(*c*) an 'Edge 2' vortex pair region that originates from the top surface of the exit lip.

A fourth vortex pair region (Edge 3 vortex pair) adjacent to the top surface of the exit lip is also deduced to be present; however, owing to its small size, it is not examined further.

For the first time, this study also identifies that the jet emerging from the FPJ nozzle departs with an azimuthal trajectory in a direction opposite to the jet precession direction. In addition, the presence and evolution of the 'flow convergence' region, although reported in a previous study, is better resolved here.

C. Y. W. acknowledges the financial support of the International Postgraduate Research Scholarship and the University of Adelaide Scholarship for the project. The authors also acknowledge the financial support of an Australian Research Council Large Infrastructure and Equipment Fund (ARC-LIEF) grant towards the acquisition of the PIV system within the University of Adelaide. Finally, the authors express their gratitude to the three referees whose comments have further improved the quality of the paper.

Appendix A. Discussion of the random, systematic and phase-averaging uncertainties

Wernet & Edwards (1990) used the following equation to estimate the random measurement uncertainties in a velocity measurement in pulsed laser velocimetry:

$$\frac{\sigma_v}{v} = \sqrt{\left(\frac{\sigma_s}{\Delta s}\right)^2 + \left(\frac{\sigma_t}{\Delta t}\right)^2}, \tag{A 1}$$

where σ refers to a standard deviation of a particular parameter, v is the velocity component in the measurement plane, Δs is the displacement of the correlation peak and Δt is the time between laser pulses. Here, the subscripts s and t represent the corresponding displacements and times, respectively. Using this formula, the worst

case calibration errors in the present measurements are estimated as:

$$\frac{\sigma_s}{\Delta s} = 5 \times 10^{-4}, \tag{A 2}$$

$$\frac{\sigma_t}{\Delta t} = 0.07 \quad (\sigma_t = 0.7\,\mu\text{s}, \Delta t = 10\,\mu\text{s} - \text{jitter between laser pulses}). \tag{A 3}$$

Thus, a typical σ_v/v value is largely a function of $\sigma_t/\Delta t$ and is nominally $\pm 3.5\,\%$. This value is limited by the performance of the Brilliant Twins lasers for the present measurements in air. There would be some advantages in using a larger Δt for the experiments for the same flow conditions, but this would mean having more particles moving out of the plane of the lightsheet causing the loss of correlation pairs leading to a loss in correlation value (Adrian 1991). Another approach would be to increase the thickness of the lightsheet. However, this would reduce the spatial resolution of the system and result in reduced scattering signals from the seed particles. This ultimately reduces the vector data yield in the region of interest, especially in those times (and/or those regions) where the jet moves out of the plane of the lightsheet.

Another potential source of error is due to curvature effects in the flow. The PIV technique approximates a curved path as the straight line between the two end points of a curvilinear path in the measurement plane. It therefore wrongly estimates the velocity magnitude and direction of the particle travelling along a curved path. The magnitude of this effect is estimated by taking the most severe case of the precession when using $\Delta t = 15\,\mu\text{s}$ (for a maximum particle movement of 0.2 mm), a typical precession frequency of 6 Hz at $x'/D_2 = 0.11$ and at a radius of 32 mm from the nozzle axis. In this case, the particle at that location will move only by 0.36° around the 32 mm radius. To a first approximation, the particles moving in a straight line will be equivalent to particles moving in an arc for such a small angle. Thus, the errors introduced by curvature effects caused by the main flow in the present measurements are negligible.

Further sources of PIV r.m.s. fluctuating velocity uncertainties using Monte Carlo simulation are detailed in Raffel, Willert & Kompenhans (1998). These uncertainties are affected by the particle image diameter, particle image displacement, ratio of particle image size and pixel size, particle image shift, image quantization, background noise of the image, displacement gradients and out-of-plane motions. Raffel *et al.* (1998) have produced general graphs for different sizes of interrogation windows, such that an approximate r.m.s. fluctuating velocity uncertainty for each measurement was possible. A typical uncertainty value for the present PIV experiments is approximately $\pm 0.7\,\text{m}\,\text{s}^{-1}$ relative to a bulk inlet velocity of $55\,\text{m}\,\text{s}^{-1}$ (or $\pm 0.013 u_i$).

The errors associated with the phase-averaging technique are mainly caused by the phase lag of the initial low-pass filtering of the hot wires and the random errors due to the inability of the probe to resolve the jet's emerging angle. Low-pass filtering introduces a finite time lag on the results relative to the actual measurements. Reducing the filter frequency increases the phase lag between the actual trigger event and the sampling event. Increasing the filter frequency past 30 Hz introduces too much high-frequency noise to the Schmitt triggers, which may activate the PIV system at an inappropriate time. For the phase-precession-direction resolved PIV experiments, the filter frequency of 30 Hz introduces a phase lag of 18° for $f_p = 3$ Hz and 36° for $f_p = 6$ Hz. This is within the assumption that a change in precession direction does not occur during this range of phase angles. The phase jitter or error band can be estimated by the same techniques as described in Wong *et al.* (2004). A typical result is presented in figure 18 which estimates that the phase-jitter (estimated from

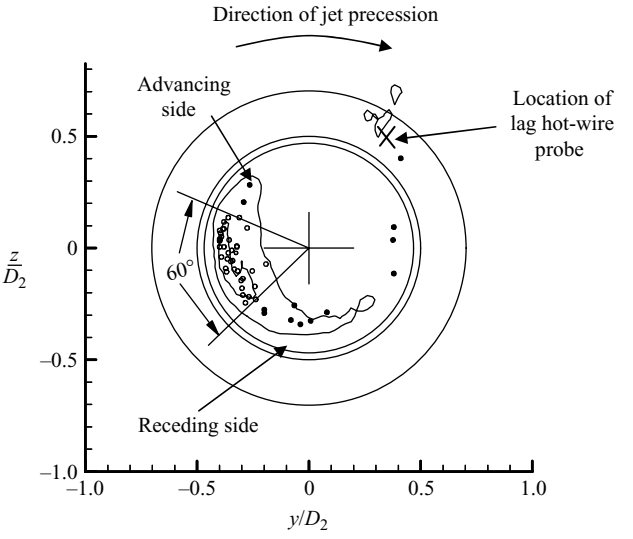

FIGURE 18. Estimation of the phase-jitter based on the estimated location of the peak in-plane velocities for the phase-and-precession-direction-resolved PIV experiments. Closed symbols are data within the 60° phase-jitter segment, while open symbols are for data outside of this segment. The larger and smaller kidney-shaped outlines represent the 0.5 and $0.9(v^2 + w^2)^{1/2}_{max}$ contours of the ensemble-averaged results of 50 image pairs. $Re_d = 59\,000$, $St_d = 0.00117$.

the location of the peak in-plane magnitude of velocity) for the present technique is approximately $\pm 30°$ about a mean jet core position for 35 out of 50 image pairs collected. In other words, approximately 75 % of the data collected are within a phase angle of $\pm 30°$ from the mean jet core position. As expected, this phase-angle jitter is much larger than in the results from a mechanically precessing jet (Schneider *et al.* 1997*b*) since the natural FPJ flow is much more variable.

The variability in the angle of the emerging jet can be estimated by inspection of the half maximum velocity contour plots for 20 phase-averaged realizations at $\eta = 30°$ presented in figure 19. The results show that only a small variance in the angle of the emerging jet exists for the phase-precession-direction resolved PIV measurements. The mean emerging angle, $\theta = 53°$ is almost constant within $x' = 40$ mm (or $x'/D_2 = 0.625$). Based on the $0.5(u^2 + v^2)^{1/2}_{max}$ contours, the range of emerging angles is estimated to be about $\pm 15°$ about the local jet centreline. This range of angles is half the value of the phase uncertainty ($\pm 30°$) of the azimuthal direction in the (y, z)-plane.

Maximum statistical uncertainty for a 95 % confidence interval based on 50 image pairs for these measurements were also calculated. For measurements in the transverse section ((y, z)-plane), the largest errors were not more than $0.032u_i$, while the minimum errors were not less than $0.001u_i$. For measurements in the longitudinal sections ((x',r)-plane), these errors were $0.022u_i$ and $0.001u_i$, respectively.

In general, variations in the phase and jet exit angle combine to reduce the peak magnitudes of phase-averaged velocities and of the velocity gradients in the flow, compared with the instantaneous jet velocities. In addition, these errors contribute to the 'smearing' of the patterns seen in the results illustrated in § 3, and to reducing the 'sharpness' of their features. This may explain why the magnitudes of the phase-averaged velocities are generally much lower than the instantaneous or even the conditionally processed results (Wong *et al.* 2002).

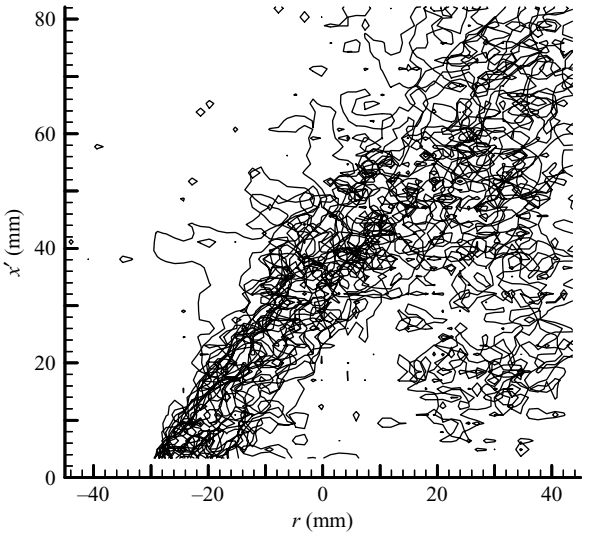

FIGURE 19. Half velocity $(0.5(v^2 + w^2)^{1/2}_{max})$ contour plots for 20 phase-averaged realizations at $\eta = 30^\circ$. $Re_d = 59\,000$, $St_d = 0.00117$.

REFERENCES

ADRIAN, R. J. 1991 Particle-imaging techniques for experimental fluid mechanics. *Annu. Rev. Fluid Mech.* **23**, 261–304.

CALVERT, J. R. 1967 Experiments on the flow past an inclined disk. *J. Fluid Mech.* **29**, 691–703.

CANTWELL, B. & COLES, D. 1983 An experimental study of entrainment and transport in the turbulent near wake of a circular cylinder. *J. Fluid Mech.* **136**, 321–374.

CROW, S. C. & CHAMPAGNE, F. H. 1971 Orderly structure in jet turbulence. *J. Fluid Mech.* **48**, 547–591.

FICK, W., GRIFFITHS, A. J. & O'DOHERTY, T. 1997 Visualisation of the precessing vortex core in an unconfined swirling flow. *Opt. Diagnost. Engng* **2**, 19–31.

FRIC, T. F. & ROSHKO, A. 1994 Vortical structure in the wake of a transverse jet. *J. Fluid Mech.* **279**, 1–47.

GUO, B. Y., LANGRISH, T. A. G. & FLETCHER, D. F. 2001 Numerical simulation of unsteady flow in axisymmetric sudden expansions. *Trans. ASME I: J. Fluids Engng* **123**, 574–587.

HART, D. P. 2000 PIV error correction. *Exps. Fluids* **29**, 13–22.

HUNT, J. C. R., ABELL, C. J., PETERKA, J. A. & WOO, H. 1978 Kinematical studies of the flows around free or surface mounted obstacles; applying topology to flow visualization. *J. Fluid Mech.* **86**, 179–200.

HUSSAIN, A. K. M. F. & REYNOLDS, W. C. 1972 The mechanics of an organized wave in turbulent shear flow. Part 2. Experimental results. *J. Fluid Mech.* **54**, 241–261.

KELSO, R. M. 2001 A mechanism for jet precession in axisymmetric sudden expansions. In *Proc. 14th Australasian Fluid Mech. Conf.* (ed. B. B. Dally), vol. 2, pp. 829–832. The University of Adelaide, Australia.

KELSO, R. M., LIM, T. T. & PERRY, A. E. 1996 An experimental study of round jets in cross-flow. *J. Fluid Mech.* **306**, 111–144.

MANIAS, C. G. & NATHAN, G. J. 1994 Low NO_x clinker production. *World Cement* **25** (5), 54–56.

MI, J. & NATHAN, G. J. 2004 Self-excited jet precession Strouhal number and its influence on turbulent mixing characteristics. *J. Fluids Struct.* **19**, 851–862.

MI, J. & NATHAN, G. J. 2005 Statistical analysis of the velocity field in a mechanical precessing jet flow. *Phys. Fluids* **17**(1), 015102.

MI, J., NATHAN, G. J. & WONG, C.Y. 2006 The influence of inlet flow condition on the frequency of self-excited jet precession. *J. Fluids Struct.* **22**, 129–133.

Nakamura, Y. & Fukamachi, N. 1991 Visualisation of flow past a frisbee. *Fluid Dyn. Res.* **7**, 31–35.

Nathan, G. J. 1988 The enhanced mixing burner. PhD thesis, Department of Mechanical Engineering, University of Adelaide, Australia.

Nathan, G. J., Luxton, R. E. & Smart, J. P. 1992 Reduced NO_x emissions and enhanced large scale turbulence from a precessing jet burner. In *Proc. 24th Symp. on Combustion*, pp. 1399–1405. The Combustion Institute.

Nathan, G. J., Turns, S. R. & Bandaru, R. V. 1996 The influence of jet precession on NO_x emissions and radiation from turbulent flame. *Combust. Sci. Technol.* **112**, 221–230.

Nathan, G. J., Hill, S. J. & Luxton, R. E. 1998 An axisymmetric 'fluidic' nozzle to generate jet precession. *J. Fluid Mech.* **370**, 347–380.

Nathan, G. J., Mi, J., Alwahabi, Z. T., Newbold, G. J. R. & Nobes, D. S. 2006 Impacts of a jet's exit flow pattern on mixing and combustion performance. *Prog. Energy Combust. Sci.* **32**, 496–538.

Newbold, G. J. R. 1997 The mixing and combustion characteristics of a precessing jet nozzle. PhD thesis, Department of Mechanical Engineering, University of Adelaide, Australia.

Newbold, G. J. R., Nobes, D. S., Alwahabi, Z. T., Nathan, G. J. & Luxton, R. E. 1995 The application of PIV to the precessing jet nozzle. In *Proc. 12th Australasian Fluid Mech. Conf.* (ed. R. W. Bilger), pp. 395–398. Sydney, Australia.

Newbold, G. J. R., Nathan, G. J. & Luxton, R. E. 1997 The large scale dynamic behaviour of an unconfined precessing jet flame. *Combust. Sci. Technol.* **126**, 71–95.

Nobes, D. N., Newbold, G. J. R., Hasselbrink, E. F., Su, L., Mungal, M. G. & Nathan, G. J. 2002 PIV and PLIF measurements in precessing and round jets. *Tech. Rep.* Dept. Mech. Engng, University of Adelaide, Australia.

Parham, J. J., Nathan, G. J., Hill, S. J. & Mullinger, P. J. 2005 A modified Thring-Newby scaling criterion for confined, rapidly-spreading and unsteady jets. *Combust. Sci. Technol.* **177**, 1421–1427.

Perry, A. E. & Chong, M. S. 1987 A description of eddying motions and flow patterns using critical-point concepts. *Annu. Rev. Fluid Mech.* **19**, 125–155.

Potts, J. R. & Crowther, W. J. 2000 Application of flow control to a disc-wing UAV. In *Proc. 16th Bristol UAV Systems Conf.* U.K.

Raffel, M., Willert, C. & Kompenhans, J. 1998 *Particle Image Velocimetry – A Practical Guide*. Springer.

Rockwell, D. 2000 Imaging of unsteady separated flows: global interpretation with particle image velocimetry. *Exps. Fluids (Suppl.)* pp. S255–S273.

Schneider, G. M., Nathan, G. J., Luxton, R. E., Hooper, J. D. & Musgrove, A. R. 1997*a* Velocity and Reynolds stresses in a precessing jet flow. *Exps. Fluids* **22**, 489–495.

Schneider, G. M., Froud, D., Syred, N. & Nathan, G. J. 1997*b* Velocity measurements in a precessing jet flow using a three dimensional LDA system. *Exps. Fluids* **23**, 89–98.

Smith, N. L., Megalos, N. P., Nathan, G. J. & Zhang, D. K. 1998 Precessing jet burners for stable and low NO_x pulverised fuel flames – preliminary results from small scale trials. *Fuel* **77**, 1013–1016.

Steiner, T. R. & Perry, A. E. 1987 Large-scale vortex structures in turbulent wakes behind bluff bodies. Part 2. *J. Fluid Mech.* **173**, 271–298.

Syred, N. 2006 A review of oscillation mechanisms and the role of the precessing vortex core (PVC) in swirl combustion systems. *Prog. Energy Combust. Sci.* **32**, 93–161.

Tobak, M. & Peake, D. J. 1979 Topology of two-dimensional and three-dimensional separated flows. In *AIAA Paper* 79–1480.

Tobak, M. & Peake, D. J. 1982 Topology of three-dimensional separated flows. *Annu. Rev. Fluid Mech.* **14**, 61–85.

Wang, K. C. 1997 Features of three-dimensional separation and separated flow structure. In *Laminar Boundary Layers* (ed. H. Schmitt), vol. 11, pp. 1–33. Computational Mechanics.

Wernet, M. P. & Edwards, R.V. 1990 New space domain processing technique for pulsed laser velocimetry. *Appl. Opt.* **29**, 3299–3417.

Wong, C. Y., Nathan, G. J. & Kelso, R. M. 2002 Velocity measurements in the near-field of a fluidic precessing jet flow using PIV and LDA. In *Proc. 3rd Australian Conf. on Laser Diagnostics in Fluid Mech. and Combustion*, pp. 48–55. University of Queensland, Brisbane, Australia.

Wong, C. Y., Lanspeary, P. V., Nathan, G. J., Kelso, R. M. & O'Doherty, T. H. 2003 Phase averaged velocity in a fluidic precessing jet nozzle and in its near external field. *J. Exps. Thermal Fluid Sci.* **27**, 515–524.

Wong, C. Y., Nathan, G. J. & O'Doherty, T. 2004 The effect of initial conditions on the exit flow from a fluidic precessing jet nozzle. *Exps. Fluids* **36**, 70–81.

Zdravkovich, M. M., Flaherty, A. J., Pahle, M. G. & Skelhorne, I. A. 1998 Some aerodynamic aspects of coin-like cylinders. *J. Fluid Mech.* **360**, 73–84.